Friction

Research Article

Stability of friction-induced vibrations in water-lubricated bearings with interfacial mechanical effects

Guo Xiang[1,5], Jiliang Mo[1], Huajiang Ouyang[1], Michel Fillon[2], Guangwu Zhou[3,✉], Liwu Wang[4], Changqi Zhou[5]

Cite this article: Xiang G, Mo JL, Ouyang HJ, et al. *Friction* 2026, **14**(6): 9441206. https://doi.org/10.26599/FRICT.2025.9441206

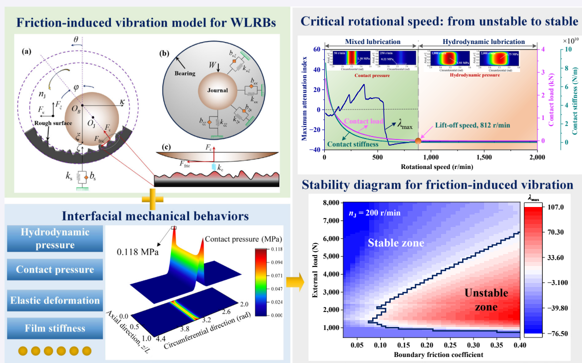

ABSTRACT: In this work, a friction-induced vibration model for water-lubricated bearings (WLBs) is developed. The model incorporates interfacial mechanical effects, including the stiffness and damping coefficients of the water film, contact stiffness of asperities, elastic deformation of the bush, etc. To evaluate the friction-induced vibration state, i.e., stability of WLBs, complex eigenvalue analysis is employed. A frictional noise experiment for a WLB is performed to validate the effectiveness of the developed model. Based on this model, the stability diagram of friction-induced vibrations in WLBs under various parameters is obtained, and the effects of key parameters, such as radial clearance, angular groove amplitude, and boundary friction coefficient, on the stability are investigated. Numerical results indicate that increasing the boundary of friction, surface roughness, radial clearance, and angular groove amplitude elevates the risk of unstable friction-induced vibration. Furthermore, numerical studies reveal the existence of a critical rotational speed at which friction-induced vibration transitions from being unstable to stable. As the rotational speed approaches the critical value, the risk of unstable friction-induced vibration rapidly decreases. Within the hydrodynamic lubrication regime, the maximum vibration attenuation index tends to remain constant, regardless of any further increases in the rotational speed.

KEYWORDS: stability analysis; friction-induced vibration; water-lubricated bearing (WLBs); interfacial mechanics

1 Introduction

Water-lubricated bearings (WLBs), as critical components, are widely employed in the stern shaft propulsion systems of submarines [1–5]. Due to the low viscosity of water and the heavy load imposed by the propeller, the hydrodynamic film formed between the propeller shaft and the WLB is often insufficient to fully separate the mating surfaces. As a result, mixed lubrication or even boundary lubrication conditions are almost inevitable in such systems [6–8]. Extensive experimental observations [9–11] have shown that under these lubrication regimes, the rotor in WLBs may generate friction-induced vibration and abnormal frictional noise, primarily caused by the nonlinear friction and contact between interfacial asperities. In the context of underwater vehicles, abnormal noise resulting from WLB systems significantly undermines the stealth and operational safety of equipment [12]. Therefore, establishing a quantitative model for friction-induced vibration and accurately evaluating the vibration stability of WLBs are crucial for optimizing their acoustic performance and guiding the design of low-noise WLB systems.

Friction-induced vibration and noise are intrinsically linked to interfacial mechanical characteristics such as friction, wear, and thermal properties [13, 14], and their underlying mechanisms are highly complex. According to the prevailing consensus in the tribology community, unstable friction-induced vibration and noise are primarily attributed to three mechanisms: a negative friction–velocity slope [15], stick-slip dynamics [16–18], and mode coupling [19–24]. Additionally, Ouyang et al. [25, 26] found that moving loads and uncertainties (primarily caused by friction, contact, wear, and thermal effects) are also significant factors contributing to unstable friction-induced vibrations. Recently, Chen et al. [27] proposed a new fundamental mechanism of friction-induced vibration and noise for dry contacting contact, which is the repeated cycles of partial detachment and then

[1] College of Mechanical Engineering, Southwest Jiaotong University, Chengdu 610031, China. [2] Prime Institute, CNRS, University of Poitiers, TSA41123, Poitiers Cedex 86073, France. [3] School of Aeronautics and Astronautics, Sichuan University, Chengdu 610065, China. [4] State Key Laboratory of Marine Resource Utilization in South China Sea, Hainan University, Haikou 570228, China. [5] School of Mechanical and Power Engineering, Chongqing University of Science and Technology, Chongqing 401331, China.

✉ Corresponding author. E-mail: gwzhou@scu.edu.cn

Received: July 30, 2025; Revised: November 24, 2025; Accepted: December 15, 2025

Nomenclature

$\boldsymbol{A}$	Damping-mass matrix	$p_{\mathrm{h}0}$	Hydrodynamic pressure at the equilibrium position, MPa
A_{nom}	Nominal contact area, m^2	R_{B}	Bearing radius, m
A_{v}	Coefficient of surface roughness	R_{J}	Journal radius, m
$\boldsymbol{B}$	Stiffness-mass matrix	t	Simulation time, s
$b_{\xi\xi}$, $b_{\kappa\kappa}$, $b_{\xi\kappa}$, and $b_{\kappa\xi}$	Damping coefficients, N·s/m	Δt	Time step, s
b_{s}	Supporting damping, N/m	W	External load, N
$B_{\mathrm{h}\kappa}$, $B_{\mathrm{h}\xi}$, $B_{\mathrm{h}\kappa'}$, and $B_{\mathrm{h}\xi'}$	Left terms of perturbed Reynolds equation	$\boldsymbol{X}$, $\dot{\boldsymbol{X}}$, and $\ddot{\boldsymbol{X}}$	Displacement, velocity, and acceleration vectors
$\boldsymbol{C}$	Damping coefficient matrix, N·s/m	y	Axial direction
C	Radial clearance, m	$\Delta\xi$, $\Delta\kappa$, and $\Delta\zeta$	Perturbed displacement, m
D	Asperity density	$\Delta\xi'$, $\Delta\kappa'$, and $\Delta\zeta'$	Perturbed velocity, m/s
e	Eccentricity, m	$\Delta\xi''$, $\Delta\kappa''$, and $\Delta\zeta''$	Perturbed acceleration, m/s^2
E_{B}	Bearing elastic modulus, GPa	ϕ	Attitude angle, °
E_{c}	Composite elastic modulus, GPa	θ	Circumferential angle, °
$F_{\mathrm{h}\kappa 0}$ and $F_{\mathrm{h}\xi 0}$	Hydrodynamic force in the horizontal and vertical directions at the equilibrium position, N	θ_{gro}	Angular groove amplitude, z
$F_{\mathrm{c}\kappa}$ and $F_{\mathrm{c}\xi}$	Contact forces in the horizontal and vertical directions, N	ϕ_θ and ϕ_y	Flow factors in circumferential and axial directions
$F_{\mathrm{fric}\kappa}$	Transient friction force in the horizontal direction, N	ϕ_{s} and ϕ_{c}	Shear and contact factors
f	Sampling frequency, Hz	ω_{J}	Angular speed, rad/s
$f_i\,(i=1\text{–}6)$	Vibration frequency, Hz	σ	Surface roughness, μm
h	Film thickness, μm	σ_{s}	Root mean square (RMS) value of rough surface height, μm
h^*	Dimensionless film thickness	(κ_0, ξ_0)	Equilibrium position of the journal
h_0	Film thickness at the equilibrium position, m	ρ	Water density, kg/m^3
h_{geo}	Geometric film thickness, μm	η	Water viscosity, Pa·s
h_{d}	Elastic deformation, μm	β	Curvature radius of asperity, m
h_{gro}	Groove depth, m	ω	Interference, m
H_{B}	Bearing hardness, Pa	ω_{c}	Critical interference, m
$k_{\xi\xi}$, $k_{\kappa\kappa}$, $k_{\xi\kappa}$, and $k_{\kappa\xi}$	Stiffness coefficients, N/m	ω_{c}^*	Dimensionless critical interference
k_{s}	Supporting stiffness, N/m	$\omega_i\,(i=1\text{–}6)$	Modal frequency, Hz
k_{c}	Contact stiffness, N/m	υ_{B}	Poisson's ratio of bush
K	Material constant	$\phi^*(z^*)$	Dimensionless rough surface probability density function
$\overline{K}$	Dimensionless stiffness coefficient	μ_{c}	Boundary friction coefficient
$\boldsymbol{K}$	Stiffness matrix, N/m	ε	Eccentricity ratio
L	Bearing width, m	$\tau_i\,(i=1\text{–}6)$	Complex eigenvalue
m_{J}	Journal mass, kg	$\lambda_i\,(i=1\text{–}6)$	Attenuation index
m_{b}	Bearing mass, kg	$\lambda_{\max}$	Maximum attenuation index
M_{cr}	Dimensionless critical mass	γ	Surface orientation
$\boldsymbol{M}$	Mass matrix, kg	δ	Viscous damping ratio of bush
n_{J}	Rotational speed of journal, r/min	δ_{h}	Surface displacement, m
q	Perturbation displacement function, m	Ω_{c}	Space frequency, Hz
O_{J}, O_{B}	Centers of journal and bearing	γ_1	PSD coefficient
p	Pressure, Pa	Ω_{cr}	Dimensionless critical speed
p_{h}	Hydrodynamic pressure, MPa		

reattachment of the contact surface. Subsequently, Chen et al. [28] employed a lead zirconate titanate (PZT)-based absorber and energy harvester (PAEH) for passive control of friction-induced stick-slip vibration in a friction system. In WLB applications, the friction behavior is significantly affected by the hydrodynamic lubrication performance, and therefore, the negative friction–velocity slope mechanism fails to accurately predict the occurrence of abnormal frictional noise in WLB systems, as it neglects the nonlinear characteristics of the friction coefficient in lubricated systems [15]. The stick-slip mechanism is characterized by the cyclic transition between sticking and slipping at the contact interface. Han and Lee [17] experimentally demonstrated that stick-slip friction is a key factor contributing to unstable friction-induced vibration in WLBs and conducted a stability analysis using a 2-degree-of-freedom (2-DOF) dynamic model. Subsequently, Qin et al. [18] experimentally observed the occurrence of stick-slip behavior and friction-induced vibration at the interface between rubber and ZQSn10-2 brass. However, the stick-slip mechanism primarily focuses on the local frictional behavior at the contact interface while neglecting the influence of system structure and vibration, which to some extent limits its applicability in predicting frictional noise in WLBs.

The third mechanism, mode coupling, suggests that interfacial friction induces the coalescence of adjacent frequencies (and modes) within the friction system toward a single frequency, thereby generating unstable self-excited vibration. This mechanism has been widely applied in the prediction of friction-induced vibration and noise in various tribological components, including WLB [21–24], frictional brakes [29], and gear [30] systems. In WLB applications, Lin et al. [21] developed a 3-DOF mode coupling model that incorporates perturbations from a stochastic rough surface to analyze the friction-induced vibration behavior of WLBs. In that study, complex eigenvalue analysis was employed to evaluate the stability of the friction-induced vibration in WLBs. Subsequently, the same research group [22, 23] incorporated nonlinear friction behaviors into their previously developed model [21]. In Ref. [23], they demonstrated that an increase in the friction coefficient or a convergence between transverse and longitudinal stiffness can generate unstable friction-induced vibration in WLB systems. A similar approach to that in Refs. [21–23] was also adopted in a more recent publication [24]. Unfortunately, these aforementioned studies [21–24] simplified the interfacial stiffness and damping of WLBs as linear spring constants without considering the actual interfacial mechanical behaviors under mixed lubrication, such as the stiffness and damping coefficients of the water film and the contact stiffness caused by asperity contact. Under varying operating conditions (such as rotational speed and load) and design parameters, the hydrodynamic film in WLBs exhibits different stiffness and damping characteristics [31, 32], and the contact behavior of rough surfaces also changes accordingly. It is therefore evident that incorporating interfacial mechanical behaviors into the mode coupling dynamic model, rather than assuming them as constant values, is essential for accurately predicting friction-induced vibration characteristics in WLB systems.

In the hydrodynamic lubrication regime, dynamic models of journal bearings incorporating the stiffness and damping coefficients of the hydrodynamic film were extensively developed [32–34], and stability was then evaluated using complex eigenvalue analysis [35–37]. For instance, Ren and Feng [35] numerically investigated the stability threshold speed of WLBs used in fuel cell vehicle air compressors by considering the stiffness and damping coefficients of the water film. More recently, they further studied the stability of high-speed water-lubricated journal bearings with lobe pockets [36]. Ren and Feng [36] analyzed the influence of microgroove geometry on the dynamic characteristics and stability of WLBs. Their findings [36] demonstrated that longer and shallower microgrooves can improve the stability of WLBs. Notably, in the mixed lubrication regime, the contact stiffness from asperity interactions is comparable to, or even exceeds, the direct water film stiffness of WLBs [38]. Undoubtedly, the contact stiffness, governed by the mixed lubrication regime, significantly affects both the dynamic characteristics and vibrational stability of WLBs. In addition, experimental observations [39, 40] have revealed that friction-induced noise occurs within a specific speed range during WLB startup and shutdown. Extensive studies, numerically [41, 42] and experimentally [43, 44], demonstrated that journal bearings sequentially transition through boundary, mixed, and hydrodynamic lubrication regimes during startup, suggesting a strong correlation between unstable friction-induced vibrations/ noise and interfacial lubrication states. However, to the best of the authors' knowledge, theoretical models for predicting the stability of friction-induced vibration and noise in WLBs under mixed lubrication conditions remain unavailable. Consequently, incorporating asperity contact mechanics and frictional behaviors into the mode coupling dynamic model of WLB systems becomes essential.

The main objective of this study is to investigate the stability of friction-induced vibration in WLBs by developing a 3-DOF dynamic model. This model incorporates interfacial mechanical behaviors, including the stiffness and damping coefficients of the hydrodynamic film as well as the contact stiffness of surface asperities, thereby addressing the limitations present in existing studies. A complex eigenvalue analysis is employed to evaluate friction-induced vibration stability and construct stability diagrams for WLBs under various operating conditions and design parameters. This work enhances the understanding of friction-induced vibration mechanisms in WLBs operating under mixed lubrication conditions and provides a theoretical foundation for their low-noise optimization design.

2 Mathematical model

2.1 3-DOF friction-induced vibration model for WLBs

Figure 1 presents the geometric representation of the 3-DOF friction-induced vibration model for WLBs, where the rough surface of the bush is magnified for clearer visualization. During operation, a hydrodynamic water film forms to support the journal; however, asperity contact frequently occurs at the interface in WLB applications. To more accurately capture the friction-induced vibration behavior of the rotor within the WLB system, it is essential to incorporate the interfacial hydrodynamic film stiffness and damping, along with the asperity contact stiffness. Accordingly, Eq. (1) is formulated to describe the 3-DOF friction-induced vibration characteristics of WLBs:

$$\begin{pmatrix} m_\text{J} & 0 & 0 \\ 0 & m_\text{J} & 0 \\ 0 & 0 & m_\text{b} \end{pmatrix}\begin{pmatrix} \Delta\xi'' \\ \Delta\kappa'' \\ \Delta\zeta'' \end{pmatrix}+\begin{pmatrix} k_{\xi\xi} & k_{\xi\kappa} & 0 \\ k_{\kappa\xi} & k_{\kappa\kappa} & 0 \\ 0 & 0 & k_\text{s} \end{pmatrix}\begin{pmatrix} \Delta\xi \\ \Delta\kappa \\ \Delta\zeta \end{pmatrix}+\begin{pmatrix} b_{\xi\xi} & b_{\xi\kappa} & 0 \\ b_{\kappa\xi} & b_{\kappa\kappa} & 0 \\ 0 & 0 & c_\text{s} \end{pmatrix}\begin{pmatrix} \Delta\xi' \\ \Delta\kappa' \\ \Delta\zeta' \end{pmatrix}=\begin{pmatrix} W-F_{h\xi0}-F_{c\xi} \\ -F_{h\kappa0}-F_{c\kappa}-F_{\text{fric}\kappa} \\ F_{h\xi0}+F_{c\xi} \end{pmatrix} \tag{1}$$

where m_J and m_b are the masses of the journal and bearing, respectively. As shown in Fig. 1(a), the subscripts κ and ξ denote the horizontal and vertical directions, respectively. ζ denotes the upward vertical vibration of the bush, which is opposite to the direction ξ. k_s and c_s are the structural support stiffness and damping coefficients of the bush, respectively. W is the external normal load applied at the journal. As illustrated in Fig. 1(b), $k_{\xi\xi}$, $k_{\xi\kappa}$, $k_{\kappa\xi}$, and $k_{\kappa\kappa}$ are the stiffness coefficients of the water film. $b_{\xi\xi}$, $b_{\xi\kappa}$, $b_{\kappa\xi}$, and $b_{\kappa\kappa}$ are the damping coefficients of the water film.

In the present study, friction-induced vibration occurs near the equilibrium position of the journal, and its amplitude remains relatively small under stable vibration conditions. Therefore, the hydrodynamic force is reasonably assumed to remain constant during microvibrations. In Eq. (1), $F_{\text{h}\kappa0}$ and $F_{\text{h}\xi0}$ are the horizontal and vertical hydrodynamic forces at the equilibrium

清华大学出版社 Tsinghua University Press | SciOpen

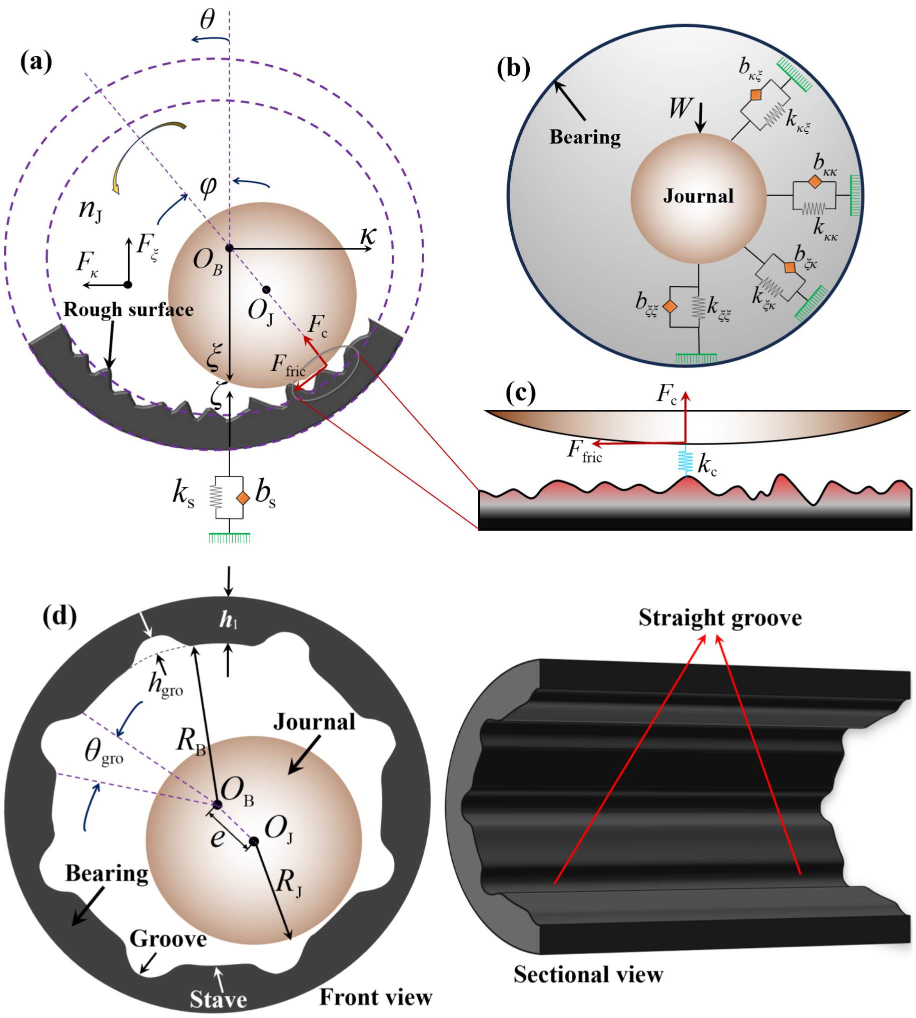

Fig. 1 Schematic diagram of 3-DOF friction-induced vibration model of WLBs considering interfacial mechanical behaviors: (a) coordinate system, (b) stiffness and damping of water film, (c) asperity contact stiffness, and (d) multigroove structure of WLB.

position, respectively. However, the transient contact forces and resulting transient friction forces during vibration cannot be neglected. In Eq. (1), $F_{c\kappa}$ and $F_{c\xi}$ are the transient horizontal and vertical contact forces caused by the rough surface, respectively. It should be noted that the friction force in the horizontal direction is much larger than that in the vertical direction. Hence, the horizontal friction force $F_{fric\kappa}$ is only considered in the friction-induced vibration model. This study investigates the friction-induced vibration of the journal relative to its equilibrium position. Therefore, the vibration displacement ($\Delta\xi$, $\Delta\kappa$, and $\Delta\zeta$), velocity ($\Delta\xi'$, $\Delta\kappa'$, and $\Delta\zeta'$), and acceleration ($\Delta\xi''$, $\Delta\kappa''$, and $\Delta\zeta''$) are all represented by Δ.

In this study, macrogrooves with millimeter-scale depths are designed to enhance heat dissipation and entrap debris, as shown in Fig. 1(d). It is noteworthy that the mixed lubrication performance at the equilibrium position governs the stiffness and damping coefficients in Eq. (1). Therefore, accurately simulating the interfacial mechanical behavior is a prerequisite for evaluating the friction-induced vibration of WLBs. Sections 2.2–2.4 detail the calculation methods for steady-state mixed lubrication, as well as the determination of stiffness and damping coefficients.

2.2 Modeling for hydrodynamic pressure, stiffness, and damping coefficients of water film

In the present study, the average Reynolds equation [44] is employed to calculate the hydrodynamic pressure of the water film in the mixed lubrication regime, which is given by Eq. (2):

$$\frac{\partial}{R_B^2\partial\theta}\left(\phi_\theta\frac{\rho h^3}{12\eta}\frac{\partial p_h}{\partial\theta}\right)+\frac{\partial}{\partial y}\left(\phi_y\frac{\rho h^3}{12\eta}\frac{\partial p_h}{\partial y}\right)=\frac{\omega_J}{2}\left(\phi_c\frac{\partial\rho h}{R_B\partial\theta}+\rho\sigma\frac{\partial\phi_s}{R_B\partial\theta}\right) \tag{2}$$

where R_B is the inner radius of the WLB. ρ and η are the density and viscosity of water, respectively. p_h and h are the hydrodynamic pressure and water film thickness, respectively. ϕ_θ and ϕ_y [44] are the flow factors in the circumferential and axial directions, respectively. ϕ_s [44] and ϕ_c [45] are the shear and contact factors, respectively. σ is the composite surface roughness. θ and y denote the circumferential and axial directions, respectively. ω_J is the angular speed of the journal, with units of rad/s. In Fig. 1, n_J is the rotational speed of the journal, with the unit being r/min. As shown in Fig. 1, the positive direction of the force is opposite to that of the fixed coordinate system of the bearing. The hydrodynamic forces in the horizontal and vertical directions at the equilibrium position can be obtained through integration, which is given by Eq. (3):

$$\begin{cases} F_{h\kappa0}=-\int_0^{2\pi}\int_0^L p_h(\theta,y)\sin\theta R_B\,\mathrm{d}\theta\mathrm{d}y \\ F_{h\xi0}=-\int_0^{2\pi}\int_0^L p_h(\theta,y)\cos\theta R_B\,\mathrm{d}\theta\mathrm{d}y \end{cases} \tag{3}$$

The Reynolds cavitation boundary condition is employed to average the Reynolds equation, which can be expressed as Eq. (4):

$$\begin{cases} p_h(\theta,0) = p_h(\theta,L) = 0 \\ p_h(\theta_0,y) = 0, \partial p_h(\theta_0,y)/\partial\theta = 0 \end{cases} \tag{4}$$

where θ_0 denotes the circumferential position at which the water film ruptures.

According to the classical perturbation method, a first-order Taylor expansion at the equilibrium position of the journal, (κ_0, ξ_0), leads to the derivation of the following perturbed average Reynolds equation, as shown in Eq. (5):

$$\left[\frac{\partial}{R_B^2\partial\theta}\left(\phi_\theta\frac{h_0^3}{12\eta}\frac{\partial}{\partial\theta}\right)+\frac{\partial}{\partial y}h_0^3\left(\phi_y\frac{1}{12\eta}\frac{\partial}{\partial y}\right)\right]p_\vartheta = B_\vartheta(h\kappa, h\xi, h\kappa', h\xi') \tag{5}$$

where h_0 is the water film thickness at the equilibrium position. $p_\vartheta(\vartheta = h\kappa, h\xi, h\kappa', \text{and } h\xi')$ represents the perturbed hydrodynamic pressure, where $\vartheta = h\kappa, h\xi$ denotes the displacement-induced perturbed hydrodynamic pressure and $\vartheta = h\kappa', h\xi'$ denotes the velocity-induced perturbed hydrodynamic pressure. The right term of Eq. (4), i.e., $B_\vartheta(\vartheta = h\kappa, h\xi, h\kappa', \text{and } h\xi')$, can be calculated as Eq. (6):

$$\begin{cases} B_{h\kappa} = \dfrac{\omega_J}{2}\left[\cos\theta - \dfrac{3\phi_\theta\sin\theta}{h_0}\dfrac{\partial h_0}{\partial\theta} - \dfrac{\phi_\theta h_0^3}{4\eta R_B^2}\dfrac{\partial p_{h0}}{\partial\theta}\dfrac{\partial}{\partial\theta}\left(\dfrac{\sin\theta}{h_0}\right)\right] \\ B_{h\xi} = -\dfrac{\omega_J}{2}\left[\sin\theta + \dfrac{3\phi_\theta\cos\theta}{h_0}\dfrac{\partial h_0}{\partial\theta} - \dfrac{\phi_\theta h_0^3}{4\eta R_B^2}\dfrac{\partial p_{h0}}{\partial\theta}\dfrac{\partial}{\partial\theta}\left(\dfrac{\cos\theta}{h_0}\right)\right] \\ B_{h\kappa'} = \sin\theta \\ B_{h\chi'} = \cos\theta \end{cases} \tag{6}$$

For the perturbed hydrodynamic pressure, the following cavitation boundary condition is used, as shown in Eq. (7):

$$p_\vartheta(\theta,y)(\vartheta = h\kappa, h\xi, h\kappa', \text{and } h\xi') = 0, \text{ if } p_h(\theta,y) = 0 \tag{7}$$

The perturbed hydrodynamic pressure can be obtained by numerically calculating Eq. (6), and then the stiffness and damping coefficients of the water film can be determined by Eqs. (8) and (9):

$$\begin{Bmatrix} k_{\xi\xi} & k_{\xi\kappa} \\ k_{\kappa\xi} & k_{\kappa\kappa} \end{Bmatrix} = \begin{Bmatrix} -\int_0^L\int_0^{2\pi} p_{h\xi}\cos\theta R_B \mathrm{d}z\mathrm{d}\theta & -\int_0^L\int_0^{2\pi} p_{h\kappa}\cos\theta R_B \mathrm{d}z\mathrm{d}\theta \\ -\int_0^L\int_0^{2\pi} p_{h\xi}\sin\theta R_B \mathrm{d}z\mathrm{d}\theta & -\int_0^L\int_0^{2\pi} p_{h\kappa}\sin\theta R_B \mathrm{d}z\mathrm{d}\theta \end{Bmatrix} \tag{8}$$

$$\begin{Bmatrix} b_{\xi\xi} & b_{\xi\kappa} \\ b_{\kappa\xi} & b_{\kappa\kappa} \end{Bmatrix} = \begin{Bmatrix} -\int_0^L\int_0^{2\pi} p_{h\xi'}\cos\theta R_B \mathrm{d}z\mathrm{d}\theta & -\int_0^L\int_0^{2\pi} p_{h\kappa'}\cos\theta R_B \mathrm{d}z\mathrm{d}\theta \\ -\int_0^L\int_0^{2\pi} p_{h\xi'}\sin\theta R_B \mathrm{d}z\mathrm{d}\theta & -\int_0^L\int_0^{2\pi} p_{h\kappa'}\sin\theta R_B \mathrm{d}z\mathrm{d}\theta \end{Bmatrix} \tag{9}$$

2.3 Modeling for contact stiffness and contact load at the bush-journal interface

In this study, the elastic study, contact model developed by Kogut and Etsion [46] (referred to as the KE contact model for simplicity) is employed to simulate the contact behavior at the bush-journal interface. For a Gaussian-distributed random surface, the KE contact model can determine the normal contact stiffness of a single asperity at different deformation stages (purely elastic, elastoplastic, and fully plastic), which can be calculated by Eqs. (10)–(13):

$$k_e(\omega) = 2E_c\beta^{1/2}\omega^{1/2} \tag{10}$$

$$k_{ep1}(\omega) = \frac{2}{3}\times 1.03\pi K H_B \times 1.425\left(\frac{\omega}{\omega_c}\right)^{0.425} \tag{11}$$

$$k_{ep2}(\omega) = \frac{2}{3}\times 1.4\beta\pi K H_B \times 1.263\left(\frac{\omega}{\omega_c}\right)^{0.263} \tag{12}$$

$$k_p(\omega) = 2\pi\beta H_B \tag{13}$$

where k_e and k_p are the contact stiffness of a single asperity in the pure elastic and plastic regimes, respectively. k_{ep1} and k_{ep2} are the contact stiffness of a single asperity in the first and second regimes of elasticfirst an deformation, respectively. E_c and H_B are the composite elastic modulus and hardness, respectively. β and ω are the curvature radius and interference of the asperity, respectively. ω_c is the critical interference, which can be calculated by Eq. (14):

$$\omega_c = \left(\frac{\pi K H_B}{2E_c}\right)^2\beta \tag{14}$$

where K is a constant related to Poisson's ratio of the bush υ_B, which can be expressed as Eq. (15):

$$K = 0.454 + 0.41\upsilon_B \tag{15}$$

The overall contact stiffness of the rough surface can be obtained by statistically integrating the stiffness contributions from individual asperities, as described in Eqs. (10)–(13). This overall contact stiffness k_c can be calculated by Eq. (16) [47]:

$$\begin{aligned} k_c(h^*) = DA_{\text{nom}}\Big\{ & 2E_c\sqrt{\beta\sigma}\int_{h^*}^{h^*+\omega_c^*}(z^*-h^*)^{1/2}\phi^*(z^*)\mathrm{d}z^* + \\ & 1.4667\times\frac{2}{3}\pi\beta K H_B\omega_c^{*(-0.425)}\int_{h^*+\omega_c^*}^{h^*+6\omega_c^*}(z^*-h^*)^{0.425}\cdot \\ & \phi^*(z^*)\mathrm{d}z^* + 1.7682\times\frac{2}{3}\pi\beta K H_B\omega_c^{*(-0.263)}\cdot \\ & \int_{h^*+6\omega_c^*}^{h^*+110\omega_c^*}(z^*-h^*)^{0.425}\phi^*(z^*)\mathrm{d}z^* + \\ & 2\pi\beta H_B\int_{h^*+110\omega_c^*}^{\infty}\phi^*(z^*)\mathrm{d}z^*\Big\} \end{aligned} \tag{16}$$

where D is the asperity density of the rough surface. A_{nom} is the nominal contact area. The superscript "*" denotes the dimensionless parameter. In Eq. (16), all the dimensionless parameters are normalized by σ. $\phi^*(z^*)$ is the rough surface probability density function, which is given by Eq. (17):

$$\phi^*(z^*) = \frac{1}{\sqrt{2\pi}}\frac{\sigma_s}{\sigma}\exp\left(-0.5\left(\frac{\sigma_s}{\sigma}\right)^2(z^*)^2\right) \tag{17}$$

where σ_s and σ are the root mean square (RMS) values of the rough surface height and asperity, respectively. According to Ref. [46], the relationship between them can be evaluated by Eq. (18):

$$\frac{\sigma_s}{\sigma} = \sqrt{1-\frac{3.717E_c-4}{(\sigma\beta D)^2}} \approx 1.0 \tag{18}$$

Notably, in the discrete solution of WLBs, the local contact stiffness at each grid point (*i*, *j*) is calculated using Eqs. (10)–(18) for its surrounding region. Subsequently, the total contact stiffness can be obtained by integrating the distributed local contact stiffness over the rough surface. In this study, the WLB operates in the mixed lubrication regime, thereby generating contact pressure at the bush surface. The contact pressure distribution of the bush surface at the equilibrium position is also determined using the KE contact model. The authors' previous study detailed the calculation method for this contact pressure distribution [48]. According to the mesoscopic-scale test results reported in Ref. [49], the contact damping ratio of rough surfaces decreases with increasing external normal load, remaining below 1% and approaching zero. Therefore, neglecting contact damping in this study is reasonable.

In this work, the microvibration of the journal is assumed to be generated from the random displacements of asperities on the bush surface. Consistent with Refs. [21, 22], a general form of the power spectral density function for railway track irregularity is adopted to generate the perturbation displacement function of the rough surface of the bush. The statistical parameters of the rough surface are incorporated into the power spectral density function, and the inverse Fourier transform is then applied to obtain the time-domain random displacement of the bush surface. Readers can refer to Refs. [21, 22] for more details. Let $q(t)$ denote the perturbation displacement function of the bush surface in the time domain. In the present study, consistent with Ref. [21], the 3D stochastic profile is simplified to a 2D stochastic profile for calculating the transient contact force $F_c(t)$, thereby facilitating the computation of asperity excitation forces and the development of a friction-induced vibration model. This assumption implies that the total contact force generated by the three-dimensional rough asperity at any given time is equivalent to the product of the overall contact stiffness and the random displacement of the two-dimensional rough asperity. Consistent with Ref. [21], the transient contact force caused by the perturbed displacement of the bush surface is characterized as Eq. (19):

$$F_c(t) = k_c(\Delta\xi + \Delta\zeta + q(t)) \tag{19}$$

As illustrated in Fig. 1, the horizontal and vertical transient contact forces can be calculated as Eq. (20):

$$\begin{cases} F_{c\kappa}(t) = k_c(\Delta\xi + \Delta\zeta + q(t))\sin\varphi \\ F_{c\xi}(t) = k_c(\Delta\xi + \Delta\zeta + q(t))\cos\varphi \end{cases} \tag{20}$$

Subsequently, the horizontal transient friction force caused by asperity contact can be evaluated by Eq. (21):

$$F_{\text{frick}}(t) = \mu_c F_c(t)\cos\varphi = \mu_c k_c(\Delta\xi + \Delta\zeta + q(t))\cos\varphi \tag{21}$$

where μ_c is the boundary friction coefficient. It should be noted that in the mixed lubrication regime, the friction force contributed by the water film is significantly smaller than that generated by asperity contact. Therefore, the hydrodynamic friction component is neglected in the proposed friction-induced vibration model.

2.4 Film thickness equation

The film thickness of the WLB is composed of elastic deformation and geometric clearance. The elastic deformation is caused by the hydrodynamic and contact pressures acting at the bush-journal interface, which increases the gap between the journal and the bush. Therefore, the film thickness equation $h(\theta, y)$ can be expressed as Eq. (22):

$$h(\theta, y) = h_{\text{geo}}(\theta, y) + h_{\text{d}}(\theta, y) + h_{\text{gro}}(\theta, y) \tag{22}$$

where $h_{\text{geo}}(\theta, y)$ and $h_{\text{d}}(\theta, y)$ are the geometrical film thickness and elastic deformations, respectively. $h_{\text{gro}}(\theta, y)$ is the groove depth, as shown in Fig. 1(d). The geometric film thickness can be obtained using Eq. (23):

$$h_{\text{geo}}(\theta, y) = C(1 + \varepsilon\cos(\theta - \varphi)) \tag{23}$$

where C is the radial clearance. ε and φ denote the eccentricity ratio and attitude angle, respectively. ε can be calculated using $\varepsilon = e/C$, where e is the distance between the journal and bearing centers, as shown in Fig. 1(d).

In the present study, the influence function method (IFM) was adopted to calculate the elastic deformation induced by hydrodynamic and contact pressures. For further details, see Ref. [50].

In this study, the bottom shape of the groove is semielliptical, as shown in Fig. 2. Since the grooves are uniformly distributed along the circumferential direction, it is only necessary to calculate the depth distribution of one groove, and the depths of the remaining grooves can be obtained through periodicity.

In Fig. 2, O and O'_0 represent the geometric centers of the WLRB and the ellipse, respectively. According to the geometric relationship shown in Fig. 2, Eqs. (24) and (25) can be obtained:

$$\frac{x_0'^2}{AO_0'^2} + \frac{y_0'^2}{O_0'C^2} = 1 \tag{24}$$

$$x_0' = -(-y_0' + OO_0')\tan(\theta') \tag{25}$$

Substituting Eq. (25) into Eq. (24), we obtain Eq. (26):

$$\begin{aligned} &(AO_0'^2 + O_0'C^2\tan^2(\theta'))y_0'^2 - 2O_0'C^2 \cdot OO_0'\tan^2(\theta')y_0' \\ &+ O_0'C^2 \cdot OO_0'^2\tan^2(\theta') - AO_0'^2 \cdot O_0'C^2 = 0 \end{aligned} \tag{26}$$

In Eq. (26), $AO_0' = R_1\sin\gamma$, $O_0'C = R_1 + h_{\text{gro}} - R_1\cos\gamma$, and $OO'_0 = R_1\cos\gamma$, where γ is half of the central angle of the groove.

Subsequently, Eq. (27) was made:

$$\begin{cases} a = AO_0'^2 + O_0'C^2\tan^2(\theta') \\ b = 2O_0'C^2 \cdot OO_0'\tan^2(\theta') \\ c = O_0'C^2 \cdot OO_0'^2\tan^2(\theta') - AO_0'^2 \cdot O_0'C^2 \end{cases} \tag{27}$$

Then, the solution for y'_0 in Eq. (26) can be written as Eq. (28):

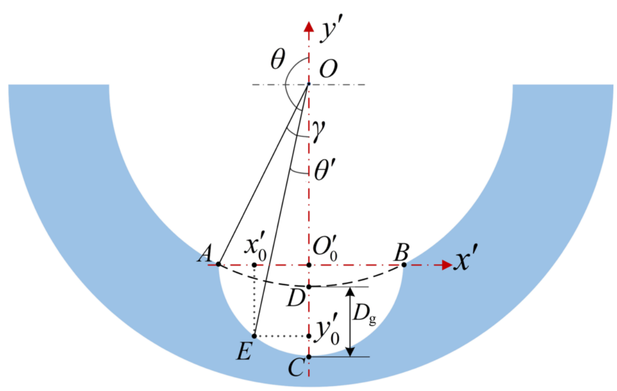

Fig. 2 Schematic diagram of groove structure.

$$y'_0 = \frac{b - \sqrt{b^2 - 4ac}}{2a} \tag{28}$$

Finally, the depth of the groove can be calculated by Eq. (29):

$$h_{\text{gro}}(\theta, y) = OE - R_{\text{B}} = \frac{R_{\text{B}} \cos \gamma - y'_0}{\cos(\theta')} - R_{\text{B}} \tag{29}$$

2.5 Complex eigenvalue analysis method

Substituting Eqs. (19)–(21) into Eq. (1), we obtain Eq. (30):

$$\begin{pmatrix} m_{\text{J}} & 0 & 0 \\ 0 & m_{\text{J}} & 0 \\ 0 & 0 & m_{\text{b}} \end{pmatrix} \begin{pmatrix} \Delta\xi'' \\ \Delta\kappa'' \\ \Delta\zeta'' \end{pmatrix} + \begin{pmatrix} k_{\xi\xi} + k_{\text{c}}\cos\varphi & k_{\xi\kappa} & k_{\text{c}}\cos\varphi \\ k_{\kappa\xi} + k_{\text{c}}\sin\varphi + \mu_{\text{c}}k_{\text{c}}\cos\varphi & k_{\kappa\kappa} & k_{\text{c}}\sin\varphi + \mu_{\text{c}}k_{\text{c}}\cos\varphi \\ -\mu_{\text{c}}k_{\text{c}}\cos\varphi & 0 & k_{\text{s}} - \mu_{\text{c}}k_{\text{c}}\cos\varphi \end{pmatrix} \cdot \begin{pmatrix} \Delta\xi \\ \Delta\kappa \\ \Delta\zeta \end{pmatrix} + \begin{pmatrix} b_{\xi\xi} & b_{\xi\kappa} & 0 \\ b_{\kappa\xi} & b_{\kappa\kappa} & 0 \\ 0 & 0 & c_{\text{s}} \end{pmatrix} \begin{pmatrix} \Delta\xi' \\ \Delta\kappa' \\ \Delta\zeta' \end{pmatrix} = \begin{pmatrix} W - F_{h\xi 0} - k_{\text{c}}q\cos\varphi \\ -F_{h\kappa 0} - k_{\text{c}}q\sin\varphi - \mu_{\text{c}}k_{\text{c}}q\cos\varphi \\ F_{h\xi 0} + k_{\text{c}}q\cos\varphi \end{pmatrix} \tag{30}$$

Equation (30) can be written in matrix form as Eq. (31):

$$\boldsymbol{M}\ddot{\boldsymbol{X}} + \boldsymbol{C}\dot{\boldsymbol{X}} + \boldsymbol{K}\boldsymbol{X} = \boldsymbol{F} \tag{31}$$

where $\boldsymbol{X}$, $\dot{\boldsymbol{X}}$, and $\ddot{\boldsymbol{X}}$ denote vectors of displacement, velocity, and acceleration, respectively. $\boldsymbol{M}$, $\boldsymbol{C}$, $\boldsymbol{K}$, and $\boldsymbol{F}$ represent the mass, damping, stiffness, and force vectors, respectively, which can be expressed as

$$\boldsymbol{X} = \begin{pmatrix} \xi \\ \kappa \\ \zeta \end{pmatrix}, \boldsymbol{M} = \begin{pmatrix} m_{\text{J}} & & \\ & m_{\text{J}} & \\ & & m_{\text{b}} \end{pmatrix}, \boldsymbol{C} = \begin{pmatrix} b_{\xi\xi} & b_{\xi\kappa} & 0 \\ b_{\kappa\xi} & b_{\kappa\kappa} & 0 \\ 0 & 0 & c_{\text{s}} \end{pmatrix},$$

$$\boldsymbol{K} = \begin{pmatrix} k_{\xi\xi} + k_{\text{c}}\cos\varphi & k_{\xi\kappa} & k_{\text{c}}\cos\varphi \\ k_{\kappa\xi} + k_{\text{c}}\sin\varphi + \mu_{\text{c}}k_{\text{c}}\cos\varphi & k_{\kappa\kappa} & k_{\text{c}}\sin\varphi + \mu_{\text{c}}k_{\text{c}}\cos\varphi \\ -k_{\text{c}}\cos\varphi & 0 & k_{\text{s}} - k_{\text{c}}\cos\varphi \end{pmatrix},$$

and $\boldsymbol{F} = \begin{pmatrix} W - F_{h\xi 0} - k_{\text{c}}q\cos\varphi \\ -F_{h\kappa 0} - k_{\text{c}}q\sin\varphi - \mu_{\text{c}}k_{\text{c}}q \\ F_{h\xi 0} + k_{\text{c}}q\cos\varphi \end{pmatrix}$

It is demonstrated from Eq. (30) that the stiffness and damping matrices are closely related to the lubrication state of the WLB, as they directly determine the water film stiffness coefficient, damping coefficient, and contact stiffness of asperities. Notably, the damping matrix $\boldsymbol{C}$ in Eq. (31) does not satisfy the proportional damping condition, necessitating the use of the state vector method for complex eigenvalue analysis. Therefore, the following auxiliary equation is introduced as Eq. (32):

$$\boldsymbol{M}\dot{\boldsymbol{X}} - \boldsymbol{M}\dot{\boldsymbol{X}} = 0 \tag{32}$$

Combining Eq. (31) with Eq. (32), Eq. (33) can be obtained:

$$\boldsymbol{A}\dot{\boldsymbol{X}}' + \boldsymbol{B}\boldsymbol{X}' = \boldsymbol{F}' \tag{33}$$

where

$\boldsymbol{X}' = \begin{pmatrix} \boldsymbol{X} \\ \dot{\boldsymbol{X}} \end{pmatrix}_{6\times 6}$, $\boldsymbol{F}' = \begin{pmatrix} \boldsymbol{F} \\ \boldsymbol{0} \end{pmatrix}_{6\times 6}$, $\boldsymbol{A} = \begin{pmatrix} \boldsymbol{C} & \boldsymbol{M} \\ \boldsymbol{M} & \boldsymbol{0} \end{pmatrix}_{6\times 6}$, and $\boldsymbol{B} = \begin{pmatrix} \boldsymbol{K} & \boldsymbol{0} \\ \boldsymbol{0} & -\boldsymbol{M} \end{pmatrix}_{6\times 6}$.

Setting $\boldsymbol{F}' = 0$, Eq. (33) reduces to the form of a free vibration equation, which is given by Eq. (34):

$$\boldsymbol{A}\dot{\boldsymbol{X}}' + \boldsymbol{B}\boldsymbol{X}' = \boldsymbol{0} \tag{34}$$

It is assumed that the particular solution of Eq. (34) is $\boldsymbol{X}' = \Psi' \mathrm{e}^{\tau t}$. Then, substituting it into Eq. (34), we obtain Eq. (35):

$$(\tau\boldsymbol{A} + \boldsymbol{B})\Psi' = 0 \tag{35}$$

For Eq. (35), the characteristic equation is shown as Eq. (36):

$$|\tau\boldsymbol{A} + \boldsymbol{B}| = 0 \tag{36}$$

where τ is a sixth-order complex conjugate eigenvalue, which can be expressed as Eq. (37):

$$\tau_i = \lambda_i \pm \omega_i \mathrm{j} \quad (i = 1\text{–}6) \tag{37}$$

where $\omega_i = 2\pi f_i$ is the modal frequency (f_i is the vibrational frequency) and $\lambda_i (i = 1\text{–}6)$ is the attenuation index of the vibration system, reflecting its stability. Let $\lambda_{\max}$ denote the maximum attenuation index. If $\lambda_{\max}$ is larger than 0, it indicates that the system is unstable and may generate friction-induced noise. Otherwise, the system is stable and unlikely to produce frictional noise. Therefore, the sign of $\lambda_{\max}$ can be used to assess journal stability. When $\lambda_{\max}$ is positive, a larger value indicates a greater tendency toward instability. When $\lambda_{\max}$ is negative, a smaller value implies increased system stability.

Equations (5)–(18) show that the stiffness and damping coefficients of the water film, as well as the asperity contact stiffness, are closely related to the bearing parameters, including the operating conditions, structural features, and material properties. Therefore, the proposed model enables the evaluation of friction-induced vibration characteristics of WLBs across a range of operating conditions and design parameters and further allows prediction of the risk of friction-induced noise.

2.6 Numerical procedure

Figure 3 shows the numerical procedure of the proposed model. Prior to the friction-induced vibration analysis, it is necessary to obtain the steady-state solution at the equilibrium position, including the stiffness and damping coefficients of the water film and the contact stiffness. The obtained stiffness and damping coefficients are used as inputs for the subsequent friction-induced vibration model. In this study, the finite difference method (FDM) is used to calculate the steady-state and perturbed hydrodynamic pressures. The friction-induced vibration analysis consists of two parts, i.e., complex eigenvalue analysis and time-domain friction-induced vibration analysis. As shown in Fig. 3, the friction-induced vibration state of the journal—either stable or unstable—is evaluated by determining the sign of the maximum attenuation index $\lambda_{\max}$, thereby predicting the possibility of friction-induced noise. Additionally, the friction-induced vibration in the time domain is obtained using the Runge–Kutta method. It is important to note that the numerical procedure shown in Fig. 3 is only used to calculate the friction-induced vibration and stability characteristics under a specific operating condition. The main purpose of this study is to evaluate the effect of various parameters on the stability zone of the WLB. To this end, the numerical procedure illustrated in Fig. 3 is repeatedly performed under different combinations of parameters to obtain the stability diagram.

The grid independence analysis indicates that in the present study, a mesh with 160 divisions in the circumferential direction and 41 in the axial direction offers a balance between

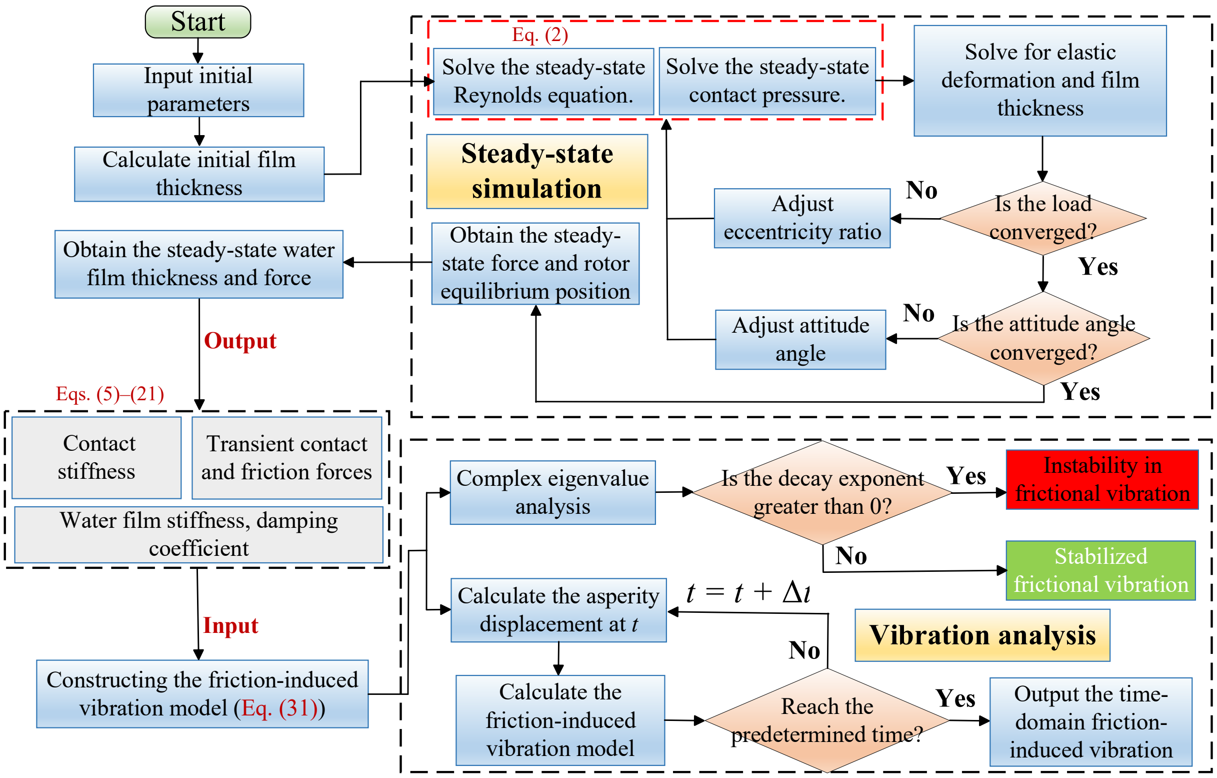

Fig. 3 Numerical procedure of present model.

computational efficiency and accuracy. In addition, the solution accuracy of the average Reynolds equation is set to 1×10^{-6}, while the convergence accuracy of the hydrodynamic force and contact force is set to 1×10^{-4}.

3 Results and discussion

3.1 Comparisons with the related works

3.1.1 Hydrodynamic performance

Accurately resolving the hydrodynamic pressure within the water film is essential for achieving reliable predictions of its interfacial mechanics and dynamic behavior. To assess the reliability of the present hydrodynamic pressure prediction, the measured pressure distributions under two external load cases for a water-lubricated bearing reported by Litwin [51] are used for comparison, as illustrated in Fig. 4. Notably, for comparison, the parameters used in the theoretical calculations are kept consistent with those adopted in the experiments. Figure 4 shows that the measured central hydrodynamic pressure along the circumferential direction agrees well with the numerical predictions. As shown in Fig. 4, the experimental hydrodynamic pressure is slightly higher than the predicted values, which may be attributed to the isothermal assumption adopted in the present model. Overall, the present theoretical model provides a reliable prediction of the hydrodynamic pressure in WLBs.

3.1.2 Dimensionless dynamic characteristics

The stiffness coefficient of the hydrodynamic film is a key parameter affecting the vibration characteristics of the journal. To verify the accuracy of the stiffness coefficient of the hydrodynamic film, the analytical solution for the hydrodynamic film stiffness of short journal bearings [52] is compared with the present numerical predictions. It is noteworthy that the journal bearing

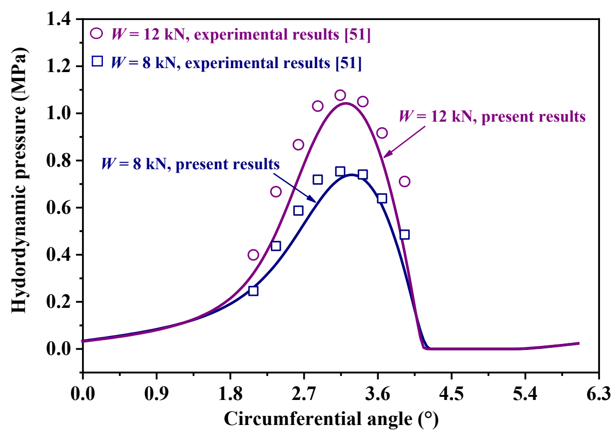

Fig. 4 Comparison of central hydrodynamic pressure distribution of WLB between present results and experimental results from Ref. [51].

described in Ref. [52] features two axial grooves, each spaced 180° apart and spanning 20° circumferentially. The length-to-diameter ratio is 2. To ensure the effectiveness of validation, the film thickness equation is modified in this study to be consistent with that in Ref. [52]. In addition, the dimensionless stiffness coefficient, $\overline{K} = kC/W$, was provided in Ref. [52], and therefore, the stiffness coefficient is normalized in the same manner as in Ref. [52]. The comparison is shown in Fig. 5(a). The measured stiffness coefficients agree well with those predicted in the present study, particularly at relatively large eccentricity ratios. However, a slight deviation between the analytical and numerical results can be observed in Fig. 5(a), particularly for the cross-coupling stiffness, $k_{\kappa\xi}$, at low eccentricity ratios (less than 0.4). This discrepancy may stem from the fact that the analytical solution for short journal bearings employs periodic boundary conditions to account for the cavitation effect, whereas the numerical calculation uses the Reynolds cavitation boundary condition. Notably, WLBs typically operate at high eccentricity ratios, often exceeding 0.98. Therefore, the present numerical model is expected to provide reliable dynamic coefficients of the hydrodynamic film.

The vibration stability of journal bearings is closely related to the stiffness and damping coefficients of the hydrodynamic film. However, the literature lacks investigations on the stability of journal bearings operating under mixed lubrication conditions. Therefore, to verify the validity of the vibration stability analysis presented in this work, the contact stiffness and boundary friction coefficient in Eq. (1) are omitted so that the friction-induced vibration model under mixed lubrication reduces to its hydrodynamic version. Subsequently, the dimensionless critical mass M_{cr} and speed Ω_{cr} predicted by the degenerated model are compared with the analytical solution for short journal bearings reported in Ref. [52]. As shown in Fig. 5(b), the present results match well with the analytical solution [52], confirming the correctness of the stability analysis of the proposed model.

By comparing the hydrodynamic pressure, film stiffness, and journal bearing stability predicted by the present model with the corresponding results reported in Refs. [51, 52], the validity of the model is preliminarily confirmed. Moreover, to directly assess the correctness of the proposed friction-induced vibration model, a frictional noise experiment for a WLB under various journal speeds and external loads is conducted, and the results are further compared with the numerical predictions. The detailed procedures and results of this experimental assessment are presented in Section 3.6.

3.2 Friction-induced vibration analysis

Table 1 lists the simulation parameters, including the structural, material, and surface properties of the WLB. In the parametric analysis (Sections 3.3–3.5), except for extending the value ranges of the analyzed factors, all other parameters are kept constant, as listed in Table 1. Notably, the model proposed in this study is applicable to WLBs with various material properties (such as Thordon, rubber, and polyetheretherketone) and geometrical dimensions, and Table 1 represents only a specific case for numerical analysis. Due to the excellent thermal conductivity of water and the heat dissipation provided by the grooves, at W = 4,050 N and n_J = 1,000 r/min, for example, the maximum temperature rise is approximately 4 °C, and the thermal deformation of the bush is only 0.3 μm, which has a negligible effect on the interfacial mechanical behavior. Although considering the temperature rise would further enhance the accuracy of the simulation, it would reduce computational efficiency. Therefore, this study adopts an isothermal assumption.

The following provides the estimation process for determining the support stiffness of the bush material. According to the Winkler assumption for an elastic foundation beam [53], the deformation displacement, δ_h, of a homogeneous material with a thickness of h_l can be calculated by Eq. (38):

$$\delta_h = \frac{p h_l (1 - \upsilon_B^2)}{E_B} \tag{38}$$

where p is the uniform pressure applied to the upper surface of the bush material and E_B is the elastic modulus of the bush. The support stiffness of the bush is defined as the force required to produce a unit displacement (1 m) in the bush material. According to Eq. (38), a displacement of 1 m requires an applied pressure of 834.1×10^9 Pa. Taking the projected area of the WLB ($2R_BL$) as the load-bearing area, the resulting load is 6.76×10^9 N.

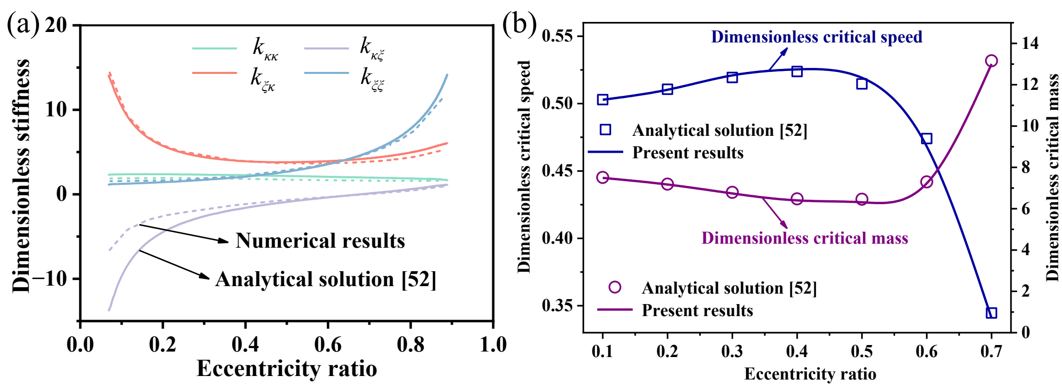

Fig. 5 Comparison of dimensionless dynamic characteristics at different eccentricity ratios: (a) dimensionless stiffness; (b) dimensionless critical speed and mass.

Table 1 Simulation parameters of WLRBs

Parameter	Value	Parameter	Value
Inner radius, R_B (mm)	45	Bearing Poisson's ratio, υ_p	0.27
Bush thickness, h_l (mm)	3	Surface orientation, γ	Isotropic
Bearing width, L (mm)	90	Bearing elastic modulus, E_B (GPa)	2.32
Radial clearance, C (mm)	0.1	Water density, ρ (kg/m^3)	1,000
Groove depth, h_{gro} (mm)	2.0	Water viscosity (20 °C), η (Pa·s)	0.001
Rotational speed, n_J (r/min)	1,000	Simulation time, t (s)	2
Angular groove amplitude, θ_{gro} (°)	10.5	Time step, Δt (s)	1×10^{-6}
Groove type	Straight	Journal mass, m_J (kg)	50
Groove number	8	Bearing mass, m_B (kg)	100
Composite surface roughness, σ (μm)	1	Supporting stiffness, k_s (N/m)	5.18×10^9
External load, W (N)	500–8,000	Damping ratio of the bush, δ	0.01

Considering that the groove area does not bear load, the resulting load after excluding the groove area is approximately 5.18×10^9 N/m. Therefore, in this study, the supporting stiffness of the bush is taken as 5.18×10^9 N/m. Additionally, the theoretical and experimental results by Sol et al. [54] indicated that the damping ratio of polymer composites is approximately 0.01. Therefore, in this study, the damping ratio of the bush material is taken as 0.01.

Table 2 summarizes the basic parameters of the stochastic rough surface. The specific physical meanings of these parameters are provided in Ref. [21]. Based on these parameters, the time-domain stochastic rough surface is generated, as shown in Fig. 6.

First, the results of the complex eigenvalue analysis of the journal under steady-state conditions with a load of 2,500 N and a rotational speed of 400 r/min are compared for boundary coefficients of friction of 0.05 and 0.3. Figure 7 shows the corresponding contact and hydrodynamic pressure distributions at the equilibrium position. It can be observed from Fig. 7(a) that the contact pressure is located at the bottom of the WLB and is relatively narrow in the circumferential direction. In addition, the

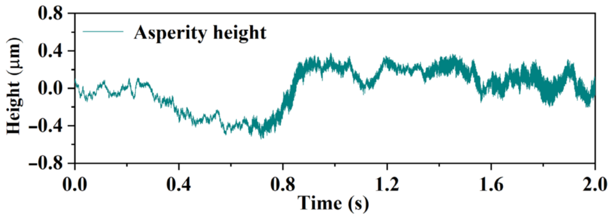

Fig. 6 Random disturbance excitation of friction interface obtained by inverting power spectral density of track irregularity.

contact pressure on both sides of the bearing is significantly higher than that at the center, which is attributed to the pressure relief at both sides of the hydrodynamic pressure region [30, 34], as shown in Fig. 7(b). In general, the WLB operates under mixed lubrication, and the stiffness and damping coefficients are as follows.

As illustrated in Table 3, the direct stiffness of the water film $k_{\xi\xi}$ is larger than the contact stiffness k_c, indicating that the hydrodynamic water film may play a dominant role in the dynamic characteristics of the WLB under the simulated working conditions.

For $\mu_c = 0.05$, the eigenvalues of the complex modal analysis are

$$\tau = \begin{pmatrix} -536949.5+0\mathrm{j} \\ -33.2-3840.4\mathrm{j} \\ -33.2+3840.4\mathrm{j} \\ -2556.4+0\mathrm{j} \\ -86.5-26.9\mathrm{j} \\ -86.5+26.9\mathrm{j} \end{pmatrix} \tag{39}$$

All the real parts of the eigenvalues are negative, indicating that the journal is in a stable friction-induced vibration state. Figures 8(a) and 8(c) plot the vibration velocity and acceleration at $\mu_c = 0.05$, respectively. As shown, the time-domain responses in all three directions exhibit stable vibration states. This result implies that the WLB is unlikely to generate abnormal friction-induced noise. Additionally, according to Eq. (36), the vibration frequencies are f_1 = 0 Hz, f_2 = 4.28 Hz, and f_3 = 611.46 Hz.

Table 2 Basic parameters of stochastic rough surface

Parameter	Value	Parameter	Value
PSD coefficient, γ_1	0.25	Coefficient of surface roughness, A_v	5.0×10^{-14}
Space frequency, Ω_c (Hz)	5,000	Time step, Δt (μs)	1
Simulation time, t (s)	2	Sampling frequency, f (Hz)	10,000

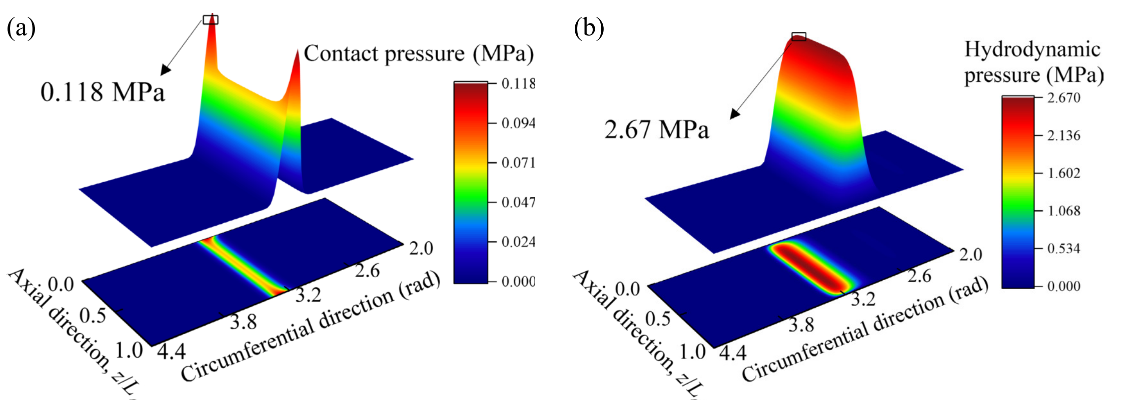

Fig. 7 Contact and hydrodynamic pressure distributions at $W = 2.5\times10^3$ N and n_J = 400 r/min: (a) contact pressure and (b) hydrodynamic pressure.

Table 3 Calculated stiffness and damping coefficients at W = 2,500 N and n_J = 400 r/min

Parameter	Value	Parameter	Value
$k_{\kappa\kappa}$ (N/m)	0.459×10^8	$k_{\xi\xi}$ (N/m)	0.18×10^{10}
$k_{\kappa\xi}$ (N/m)	0.64×10^8	$k_{\xi\kappa}$ (N/m)	0.561×10^9
$b_{\kappa\kappa}$ (N·s/m)	0.232×10^6	$b_{\xi\xi}$ (N·s/m)	0.268×10^8
$b_{\kappa\xi}$ (N·s/m)	0.163×10^7	$b_{\xi\kappa}$ (N·s/m)	0.163×10^7
k_c (N/m)	0.481×10^9		

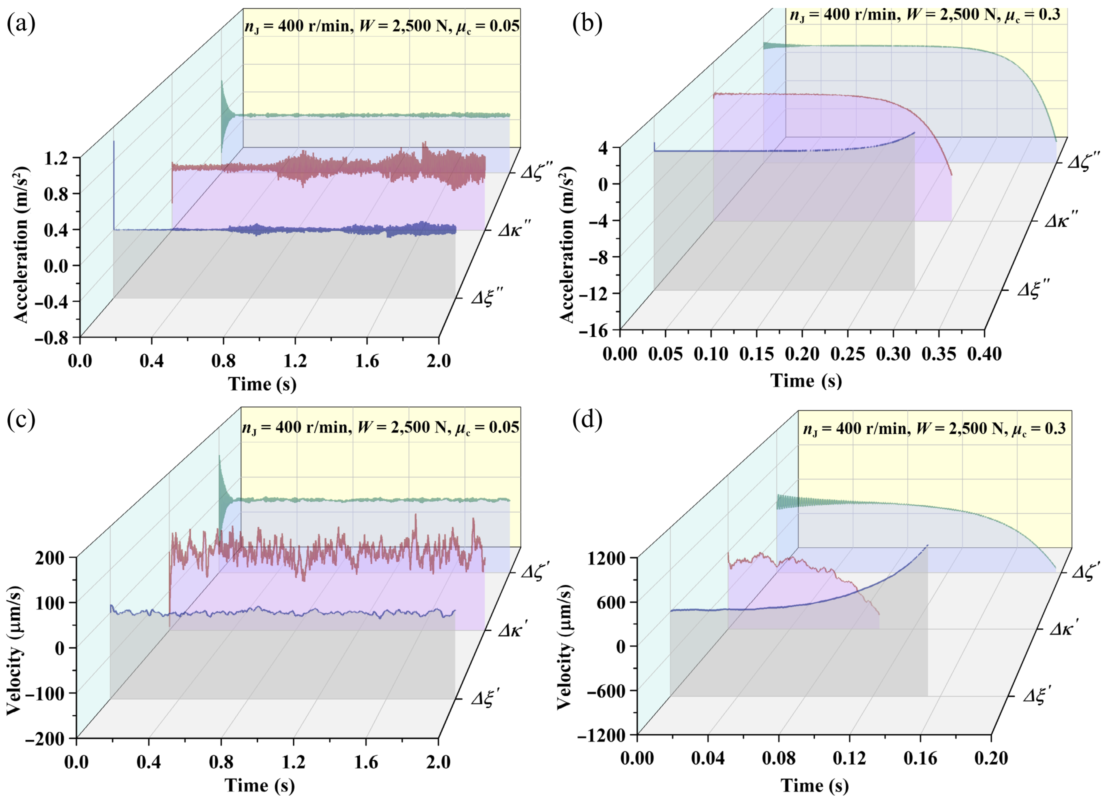

Fig. 8 Vibration velocity and acceleration of the WLB under different boundary friction coefficients: vibration velocity at (a) $\mu_c = 0.05$ and (b) $\mu_c = 0.3$; vibration acceleration at (c) $\mu_c = 0.05$ and (d) $\mu_c = 0.3$.

Notably, the damping coefficient of the water film is sufficiently large, leading to an overdamped WLB system. This ultimately results in the presence of purely real eigenvalues, as illustrated in Eq. (39).

However, as μ_c increases to 0.3, as illustrated in Eq. (40), a positive value of 29.4 appears among the complex eigenvalues, indicating that the journal will experience abnormal friction-induced vibration. In Section 3.3.1, the effect of μ_c on the stability of the journal under various external loads and rotational speeds is systematically studied.

$$\tau = \begin{pmatrix} -536949.5+0\mathrm{j} \\ -30.7-3836\mathrm{j} \\ -30.7+3836\mathrm{j} \\ -2596.9+0\mathrm{j} \\ -167.3-0\mathrm{j} \\ 29.4+0\mathrm{j} \end{pmatrix} \tag{40}$$

3.3 Effects of surface parameters

3.3.1 Boundary friction coefficient μ_c

Figure 9 shows the stability maps related to μ_c, where the horizontal axis represents the investigated parameter and the vertical axis denotes the external load under four different rotational speeds: 200, 400, 600, and 800 r/min. In Fig. 8, the black line marks the boundary between the stable and unstable zones. As shown in Fig. 9(a), at ω = 200 r/min, when μ_c is less than 0.075, the journal exhibits stable vibrations across the entire external load range of 500 to 8,000 N. However, as μ_c further increases, unstable friction-induced vibrations emerge, and the corresponding external load range broadens. This finding demonstrates that an elevated boundary friction coefficient μ_c increases the propensity for unstable friction-induced vibration to develop in WLB systems. Such behavior aligns with earlier experimental findings documented in Refs. [10–12] and theoretical models presented in Refs. [21, 23]. In particular, Ref. [21] noted that a boundary friction coefficient above 0.2 tends to trigger unstable friction-induced vibration in WLBs. The present study further reveals that at rotational speeds under 600 r/min, the probability of noise generation rises markedly once the friction coefficient surpasses this threshold. Additionally, as shown in Figs. 9(a)–9(c), when the external load varies between 500 and 8,000 N, unstable friction-induced vibrations occur only within the intermediate load range. This is because, at relatively low external loads, the WLB operates in the hydrodynamic lubrication regime, where friction-induced vibrations caused by asperities do not occur. However, at a relatively high external load, although the asperity contact increases, the damping coefficient of the water film is also large (on the order of 10^8–10^9 N·s/m), which can suppress the friction-induced amplification of rotor vibrations. As a result, the rotor exhibits stable vibrations under relatively high external loads. In fact, numerous studies [32, 35–37] have demonstrated that when asperity contact and interfacial friction at the bearing surface are neglected, journal bearing systems tend to remain absolutely stable at high eccentricity ratios (or under high external loads). However, within the intermediate load range, the energy generated by interfacial contact and friction is insufficient to be dissipated by water film damping, leading to the occurrence of unstable friction-induced vibrations.

In addition, as illustrated in Fig. 9, the unstable zone gradually shrinks as the rotational speed increases and completely disappears when the speed reaches 800 r/min. This is because the hydrodynamic lubrication performance improves with increasing rotational speed, leading to reduced asperity contact. Specifically, as shown in Fig. 9, using an external load of 3,000 N as an example, as the rotational speed increases from 200 to 800 r/min, the minimum film thickness increases from 1.14 to 2.72 μm, leading to a decrease in contact load from 357.5 to 3 N. Correspondingly, the contact stiffness decreases from 6.75×10^9 to 1.51×10^7 N/m. In addition, as shown in Fig. 10, the maximum contact pressure rapidly decreases from 0.778 to 0.01 MPa as the rotational speed increases from 200 to 800 r/min. Consequently, the likelihood of unstable friction-induced vibrations decreases as the mixed lubrication performance improves. Notably, although the rotor of the WLB exhibits fully stable friction-induced vibrations at 800 r/min, when μ_c ranges from 0.35 to 0.4 and the external load varies between 5,500 and 8,000 N, the value of λ_{max} approaches zero, indicating that the rotor is near a critically stable state.

3.3.2 Surface roughness σ

The surface roughness is a key parameter affecting the tribological performance of the contact interface. Figure 11 shows the stable maps related to surface roughness under four different rotational speeds. The area of the unstable zone decreases with increasing rotational speed, which can be attributed to enhanced hydrodynamic performance. Similar to Fig. 9, the rotor exhibits stable friction-induced vibrations at relatively high loads due to the high damping coefficient of the water film. Additionally, Fig. 11 indicates that in WLB applications, unstable friction-induced vibrations are more likely to occur on rougher surfaces. More specifically, as shown in Fig. 11(d), even when the rotational speed reaches 1,000 r/min, unstable friction-induced vibrations may still occur if the surface roughness exceeds 1.8 μm. These results can be explained by the fact that a larger σ leads to increased asperity contact, thereby generating a greater risk of unstable friction-induced vibration. This numerical result is consistent with the experimental observation in Ref. [18], which reported that an increase in contact pressure raises the risk of

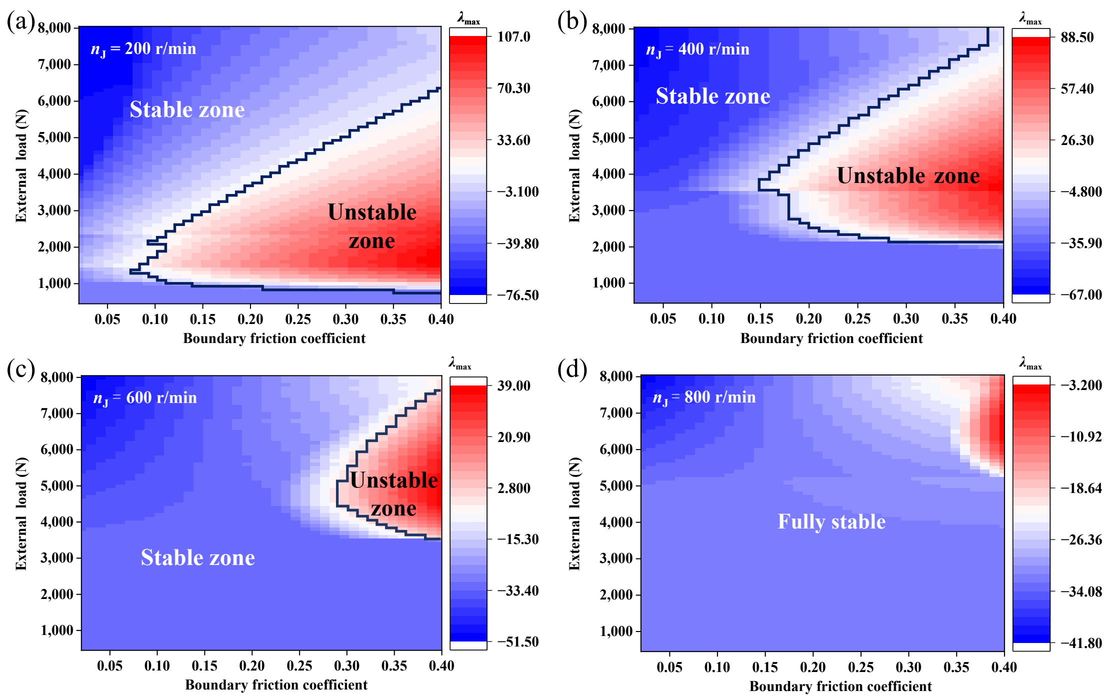

Fig. 9 Effects of boundary friction coefficient on stable zone of friction-induced vibration under different external loads at (a) 200, (b) 400, (c) 600, and (d) 800 r/min.

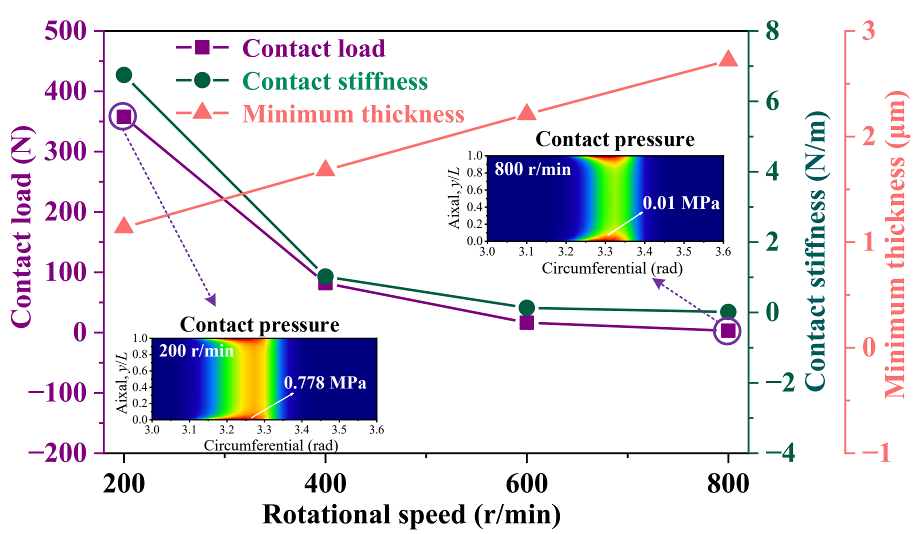

Fig. 10 Variation of contact load, contact stiffness, and minimum thickness with rotational speed at W = 3,000 N.

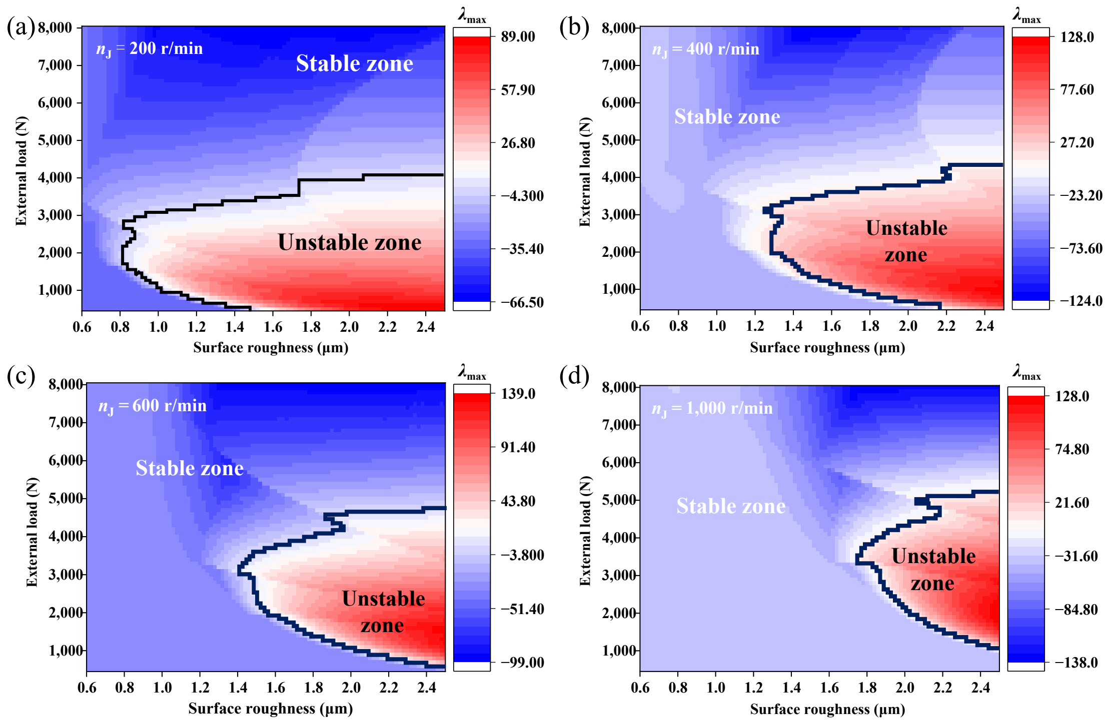

Fig. 11 Effects of surface roughness on stable zone under different external loads at (a) 200, (b) 400, (c) 600, and (d) 800 r/min.

unstable friction-induced vibration. As demonstrated in Fig. 11, the lower limit of the external load for unstable vibration gradually increases as σ decreases. This is because with increasing σ, the critical load required to achieve hydrodynamic lubrication at a given rotational speed decreases.

3.4 Effects of key structural design parameters

3.4.1 Radial clearance C

A reasonable radial clearance design is crucial for enhancing the lubrication performance of WLBs. However, the effect of radial clearance on friction-induced vibration characteristics remains unclear. The objective of this section is to reveal the effects of radial clearance on the stability of friction-induced vibration under different external loads, as shown in Fig. 12. It can be found from Fig. 12(a) that at $\omega = 200\ \mathrm{r/min}$, the load range over which unstable friction-induced vibration occurs slightly increases with increasing radial clearance. Furthermore, the value of $\lambda_{\max}$ also increases significantly with the radial clearance, indicating that the risk of instability increases as the radial clearance increases. When the rotational speed increases to 400 r/min, the unstable zone is reduced compared with that at 200 r/min, as shown in Fig. 12(b). As the rotational speed increases further, the unstable zone of friction-induced vibration disappears, as shown in Figs. 12(c) and 12(d).

These results indicate that using an excessively large radial clearance in the design of WLBs will increase the risk of friction-induced noise at low rotational speeds. Notably, bush wear increases the clearance between the journal and the bearing. According to the experimental results in Ref. [55], the increased radial clearance caused by wear can lead to unstable friction-induced vibration, a trend that agrees with the present numerical prediction. Specifically, in the current simulation, designing the radial clearance to be less than three thousandths of the radius enables the WLB to maintain stable friction-induced vibration across the entire external load range, as illustrated in Fig. 12(b). This result is consistent with the recommendation made in Ref. [56]. Notably, although a relatively small radial clearance exhibits excellent stability under the isothermal assumption, an excessively small clearance may increase the risk of chatter due to thermal expansion [57]. Future studies will consider the influence of thermal expansion effects under heavy-load conditions to more accurately assess the impact of small radial clearance on the stability of friction-induced vibration.

The evolution of the contact pressure distribution with varying radial clearance at 200 r/min and an external load of 2,050 N, as illustrated in Fig. 13, helps explain the results shown in Fig. 12(a). As illustrated in Fig. 13, increasing the radial clearance leads to intensified interfacial asperity contact and a corresponding increase in contact stiffness. More specifically, as the radial clearance increases from 0.05 to 0.25 mm, the contact load rises from 98.4 to 444 N, the contact stiffness increases from 1.6×10^9 to 6.0×10^9 N/m, and the maximum contact pressure grows from 0.12 to 1.06 MPa. This result suggests that an increase in radial clearance leads to increased asperity contact. As experimentally demonstrated in Ref. [18], the amplitude of friction-induced vibration increases markedly when the contact pressure exceeds 0.56 MPa. As shown in Fig. 13, the predicted maximum contact pressure becomes greater than 0.71 MPa once the radial clearance exceeds 0.17 mm, under which condition unstable friction-induced vibration is likely to occur, as demonstrated in Figs. 12(a) and 12(b). In addition, the direct damping coefficient of the water film $b_{\xi\xi}$ decreases from 6.57×10^7 to 1.98×10^7 as the radial clearance increases from 0.05 to 0.15 mm. These results indicate that as the radial clearance increases, the accumulated energy from asperity friction rises, while the interfacial damping of the water film decreases, thereby increasing the risk of abnormal friction-induced vibration, as shown in Figs. 12(a) and 12(b).

3.4.2 Angular groove amplitude θ_{gro}

In WLB applications, the macrogroove can lead to a loss of hydrodynamic pressure, which may in turn affect the friction-induced vibration behavior of the rotor in WLB systems. Hence, the purpose of this section is to investigate the effect of the angular

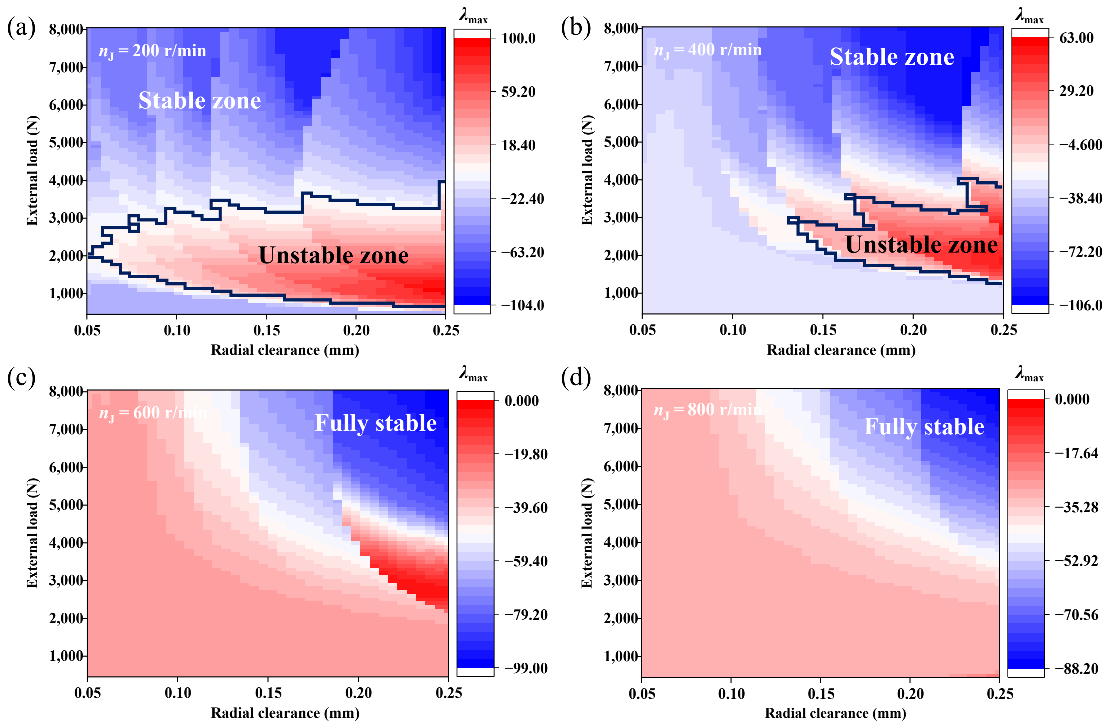

Fig. 12 Effects of radial clearance on stable zone under different external loads at (a) 200, (b) 400, (c) 600, and (d) 800 r/min.

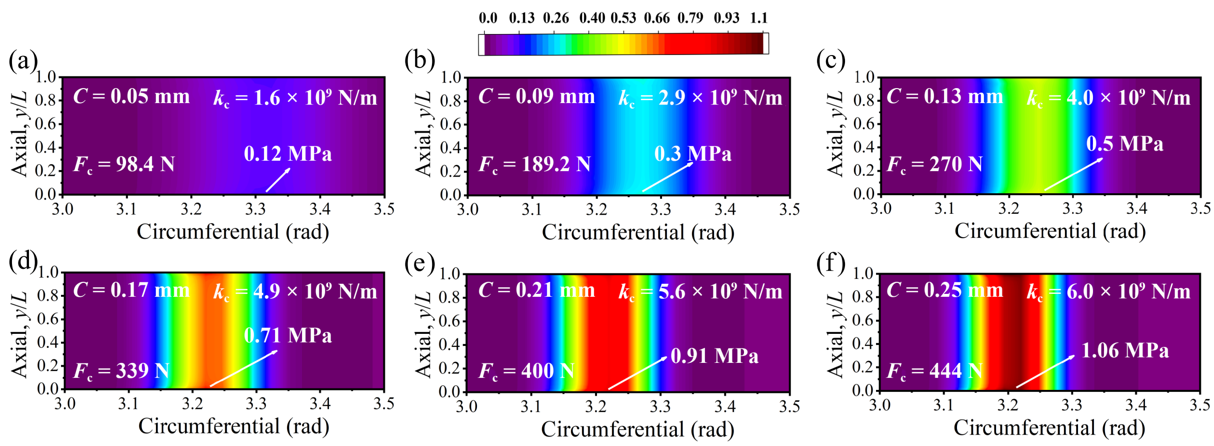

Fig. 13 Evolution of contact pressure distribution with radial clearance at ω = 200 r/min and W = 2,050 N: (a) C = 0.05 mm, (b) C = 0.09 mm, (c) C = 0.13 mm, (d) C = 0.17 mm, (e) C = 0.21 mm, and (f) C = 0.25 mm.

groove amplitude on the stability of the friction-induced vibration of WLBs. Figure 14 shows the variation in the maximum attenuation index λ_{max} with external load under different angular groove amplitudes at n_J = 400 r/min and μ_c = 0.2. As shown in Fig. 14(a), the range of external loads associated with unstable friction-induced vibration increases with angular groove amplitude. Additionally, the maximum attenuation index also increases as the angular groove amplitude increases. Hence, the results in Fig. 14(a) indicate that increasing the angular groove amplitude raises the risk of abnormal friction-induced vibration. It can be seen from Fig. 14(b) that when the angular groove amplitude exceeds 28.5°, the WLB exhibits a risk of abnormal friction-induced vibration across the entire load range of 500 to 5,000 N. For the WLB dimensions used in this study, an angular groove amplitude of 28.5° implies that the groove area is approximately 1.98 times the load-carrying area. In such a groove design, the formation of hydrodynamic pressure will be severely disrupted, making it more likely to trigger unstable friction-induced vibration. Furthermore, when the angular groove amplitude increases to 31.5°, the maximum attenuation index becomes even larger than that at 28.5°, implying a further intensification of friction-induced vibration.

Figure 15 shows the contact pressure distributions for four different angular groove amplitudes at W = 4,050 N (corresponding to the specific pressure of 0.5 MPa), i.e., θ_{gro} = 4.5 N (corr, 22.5°, and 31.5°). As demonstrated in Fig. 14, the friction-induced vibration is unstable in all four cases. Obviously, the maximum contact pressure and contact stiffness significantly increase with increasing angular groove amplitude. Specifically, the maximum contact pressure increases from 0.32 to 1.14 MPa, and the contact stiffness increases from 2.69×10^9 to 1.49×10^{10} N/m. As mentioned earlier, the rise in contact pressure is a key factor contributing to unstable friction-induced vibration in WLBs [18]. Compared with the substantial increase in contact characteristics, the direct damping coefficient of the water film $b_{\xi\xi}$ shows only a slight increase with angular groove amplitude. This suggests that as the angular groove amplitude increases, the slight increase in water film damping may be insufficient to suppress the vibration

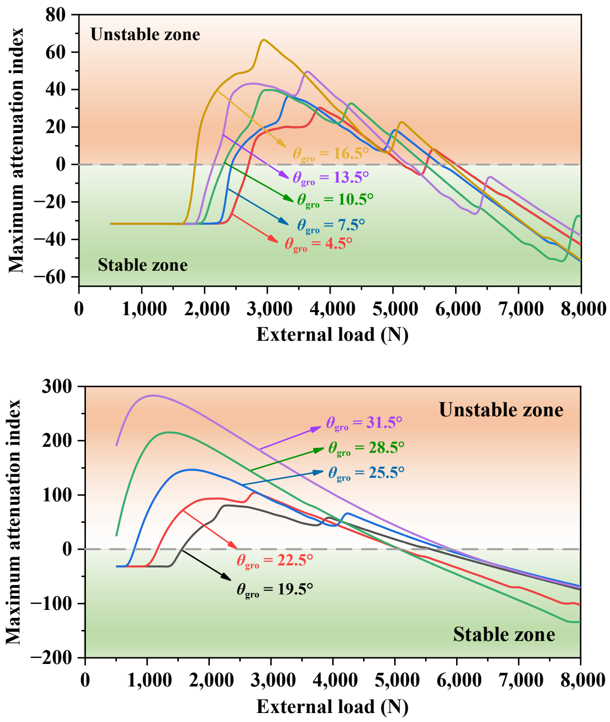

Fig. 14 Effects of groove width on the maximum attenuation index with various external loads at n_J = 400 r/min and μ_c = 0.2: (a) θ_{gro} ranging from 4.5° to 16.5°, (b) θ_{gro} ranging from 19.5° to 31.5°.

intensification caused by increased contact effects. As a result, a wider angular groove amplitude exhibits greater vibration instability. Eventually, at W = 4,050 N, the maximum attenuation index increases as the angular groove amplitude decreases, as shown in Fig. 14.

3.5 Effects of rotational speed

As demonstrated in Figs. 9, 11, and 12, the increasing rotational speed leads to a reduction in the unstable zone. This section focuses on the variation in friction-induced vibration stability of the WLB as the rotational speed continuously changes from 10 to 2,000 r/min under specific pressures of 0.25 (2,025) and 0.5 MPa (4,050 N), with μ_c of 0.2. As shown in Fig. 16(a), unstable friction-induced vibration occurs only at low speeds for both W = 2,025 N and W = 4,050 N. This finding suggests that frictional noise tends to appear more readily during the start-up phase of WLBs, which is supported by numerous experimental observations (e.g., Refs. [39, 40]). Interestingly, the maximum attenuation index of W = 2,025 N is larger than that of W = 4,050 N. This is because the direct damping coefficient of the water film at W = 4,050 N is higher than that at W = 2,025 N. As a result, under high external load, the water film suppresses abnormal vibrations more effectively than under low external load. In addition, Fig. 16(a) reveals an interesting phenomenon: at an external load of 4,050 N, the WLB exhibits stable frictional vibrations at speeds below approximately 100 r/min. This is likely because the frictional energy generated at such low speeds is insufficient to excite system instabilities, and the potential vibrations are suppressed by the damping of both the interfacial water film and the structural support, leading to a stable frictional vibration state.

Furthermore, as shown in Fig. 16(a), there exists a critical rotational speed: below this speed, unstable friction-induced vibration occurs, while above it, the system remains stable. This behavior is observed at both W = 2,025 N and W = 4,050 N. As indicated in Fig. 16(a), the corresponding critical speeds are 375 and 560 r/min, respectively. Figure 16(b) is plotted to explain the result presented in Fig. 16(a). As shown in Fig. 16(b), the contact load and stiffness first decrease rapidly with increasing rotational speed and then tend to stabilize as the rotational speed increases

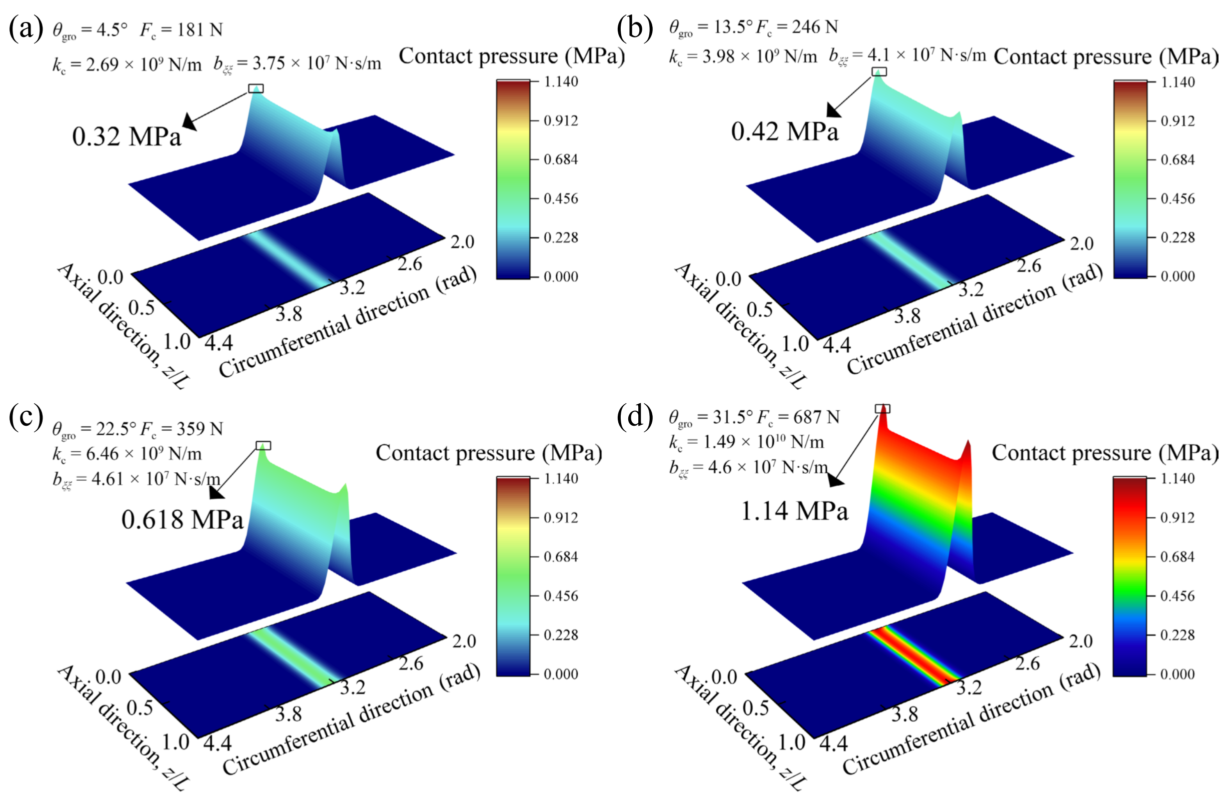

Fig. 15 Contact pressure distributions under different groove widths at n_J = 400 r/min, μ_c = 0.2, and W = 4,050 N: (a) θ_{gro} = 4.5°, (b) θ_{gro} = 13.5°, (c) θ_{gro} = 22.5°, and (d) θ_{gro} = 31.5°.

further. More specifically, the contact load and stiffness are 107 N and 1.39×10^9 N/m at the critical rotational speed of 560 r/min, respectively, implying that the WLB approaches the hydrodynamic lubrication regime. As illustrated in Fig. 16(b), the lift-off speed, defined as the point where the lubrication regime transitions from mixed lubrication to hydrodynamic lubrication, is 812 r/min, which is higher than the critical rotational speed. Therefore, it can be concluded that the stability of friction-induced vibration is closely related to the lubrication regime of the WLB. As the WLB system approaches hydrodynamic lubrication, the risk of friction-induced vibration decreases rapidly. Once hydrodynamic lubrication is achieved, the WLB exhibits absolute stability. Finally, as illustrated in Fig. 16(b), the maximum attenuation index remains unchanged once the WLB enters the hydrodynamic lubrication regime. Overall, this work presents a feasible quantitative model for determining the critical rotational speed at which abnormal friction-induced vibration disappears during the start-up of WLBs.

3.6 Experimental verification

Due to the limitations of the current experimental setup, it is difficult to isolate the coupled vibrations of the test rig, making it challenging to accurately measure the rotor vibration characteristics solely induced by rough surface excitation. Therefore, this study evaluates the stability of friction-induced vibration in the rotor by measuring the frictional noise of WLBs under various combinations of load and rotational speed. Subsequently, the effectiveness of the theoretical model is verified by comparing the results with those obtained from complex eigenvalue analysis. Figure 17 shows the overall test rig, bearing test chamber, and tested rubber bearing, corresponding to Figs. 17(a), 17(b), and 17(c), respectively.

Table 4 lists the main parameters of the tested WLB, including structural, material, and surface parameters. As demonstrated in Section 3.3.2, the surface roughness significantly affects the friction-induced vibration characteristics of the WLB. Therefore, the surface profile of the rubber is first measured using a white light interferometer to directly obtain the RMS roughness. The measured surface roughness value is 3.5 μm. According to Eq. (38), the supporting stiffness of the bush is approximately 2.2×10^7 N/m. The test results by Tiwari et al. [58] on the loss factor of rubber indicate that the loss factor reaches approximately 0.2 at a frequency of 100 Hz. Since the damping ratio of rubber is half of its loss factor, a damping ratio of 0.1 is adopted in the computational model. In this study, a hydrophone, which is made by Jiangsu Donghua Testing Technology Co., Ltd., China, is used to identify the friction noise of the tested WLB. As shown in Fig. 18, the hydrophone is immersed in the water tank and positioned close to the rubber–journal friction pair. The operating frequency range of the hydrophone is 2–30 kHz, its sensitivity is −173.0 dB V/μPa ± 2 dB, and its preamplifier gain is 40 dB.

Prior to the frictional noise tests, μ_c needs to be determined. A torque meter is employed to measure the friction torque generated by the WLB, which is then converted into the corresponding friction coefficient. The friction coefficient obtained under dry contact conditions at 10 r/min is adopted as the boundary friction coefficient. The experimentally determined values of the boundary friction coefficient under specific pressures of 0.2 and 0.3 MPa are 0.298 and 0.271, respectively.

The experiment measures the frictional noise of the WLB under two specific pressures, 0.2 and 0.3 MPa, as the rotational speed increases from 20 to 180 r/min (specifically set at 20, 40, 60, 80, 110, 140, and 180 r/min). The specific pressures of 0.2 and 0.3 MPa correspond to loads of 5.12 and 7.68 kN, respectively. The radial load is applied hydraulically, with a maximum load capacity of 50 kN and a loading accuracy of 0.06% full scale (FS). The driving motor is a 10-pole, three-phase asynchronous servo motor. The rotational speed control accuracy is approximately

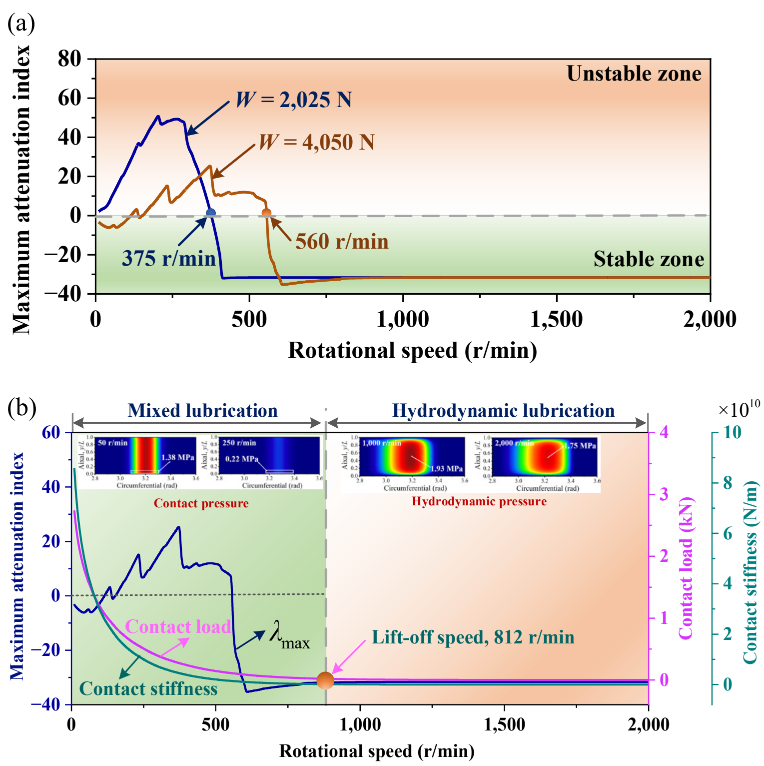

Fig. 16 Effects of rotational speed on maximum attenuation index and contact characteristics: (a) maximum attenuation index under external loads of 2,025 and 4,050 N; (b) maximum attenuation index, contact load, and contact stiffness under an external load of 4,050 N.

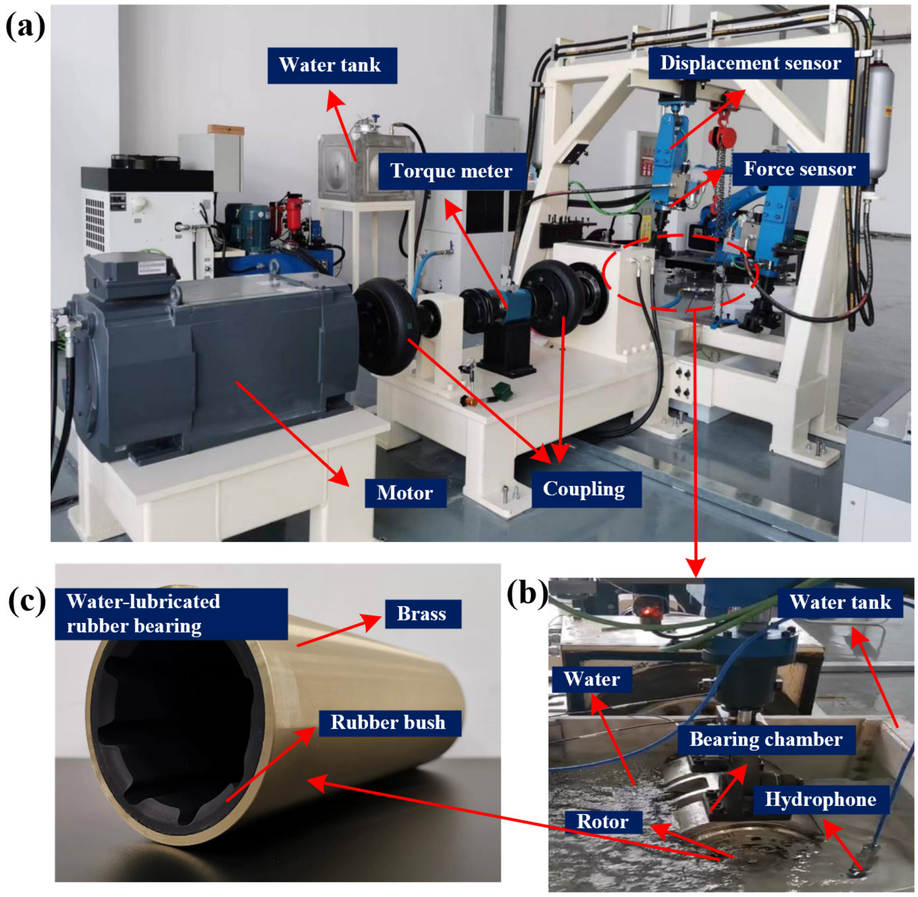

Fig. 17 Test rig schematic diagram: (a) entire test rig, (b) bearing test chamber, and (c) tested bearing.

Table 4 Parameters of tested water-lubricated bearing

Parameter	Value	Parameter	Value
Inner radius, R_B (mm)	40	Angular groove amplitude, θ_{gro} (°)	15
Bearing width, L (mm)	320	Specific pressure, p_s (MPa)	0.1–0.3
Radial clearance, C (mm)	0.15	Rubber thickness, h_l (mm)	10
Elastic modulus, E_B (MPa)	10	Groove number	8
Rotational speed, n_J (r/min)	20–200	Surface roughness, σ (μm)	3.5
Water density, ρ (kg/m^3)	1,000	Poisson's ratio of rubber, υ_p	0.47
Groove depth, D_g (mm)	5	Supporting stiffness, k_s (N/m)	2.2×10^7
Groove type	Straight	Damping ratio, δ	0.1

0.1%; for instance, at a set speed of 1,000 r/min, the actual speed ranges between approximately 999 and 1,001 r/min.

The time-domain signals collected by the acoustic sensor are analyzed using the FFT method based on spectral analysis. This provides the sound pressure amplitude (dB) in the frequency domain. If a significant peak appears at a specific frequency and the corresponding sound is continuous, the tested bearing is considered to exhibit abnormal frictional vibration noise under that test condition. The theoretical model is configured with the same parameters as the experiment, and the complex eigenvalue analysis is conducted under different combinations of rotational speeds and external loads. Subsequently, the possibility of friction-induced noise in the tested bearing is evaluated by determining the sign of the real part of the eigenvalues. Finally, the rationality of the theoretical model is verified by comparing it with friction noise tests. Notably, to ensure the repeatability of the test results, three frictional noise tests were conducted for each load and speed condition.

Figure 19 presents the experimental sound pressure signals in both the time and frequency domains under a specific pressure of 0.2 MPa, with rotational speeds ranging from 20 to 180 r/min. The results of the three frictional noise tests are consistent; therefore, only one set of tests is presented here. It is evident that abnormal frictional noise occurs at lower rotational speeds between 20 and 110 r/min but disappears at higher speeds of 140 and 180 r/min. This experimental observation aligns well with the numerical predictions shown in Fig. 16. Correspondingly, Fig. 20 illustrates the horizontal friction-induced vibration and rotor displacement predicted by the proposed model at various rotational speeds. As shown in Fig. 20, the maximum attenuation indexes are positive at 20–110 r/min (indicating instability) and negative at ω = 140 and 180 r/min (indicating stability).

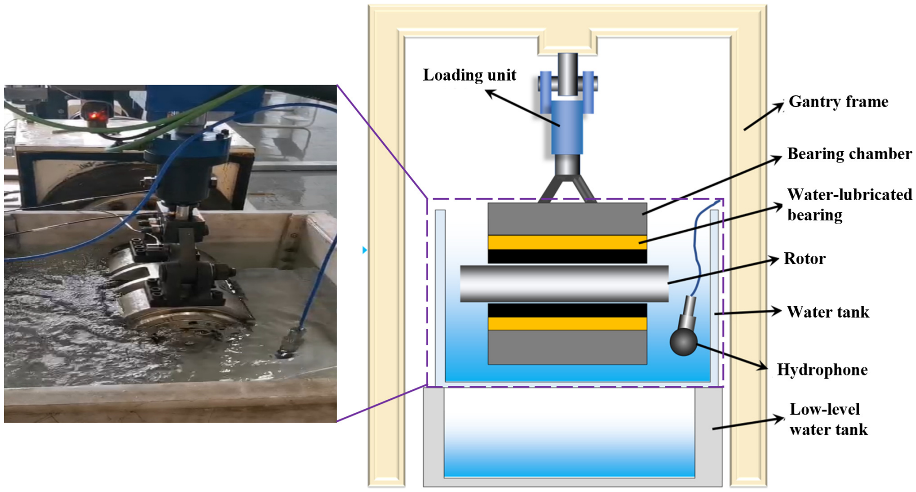

Fig. 18 Noise sensor layout diagram.

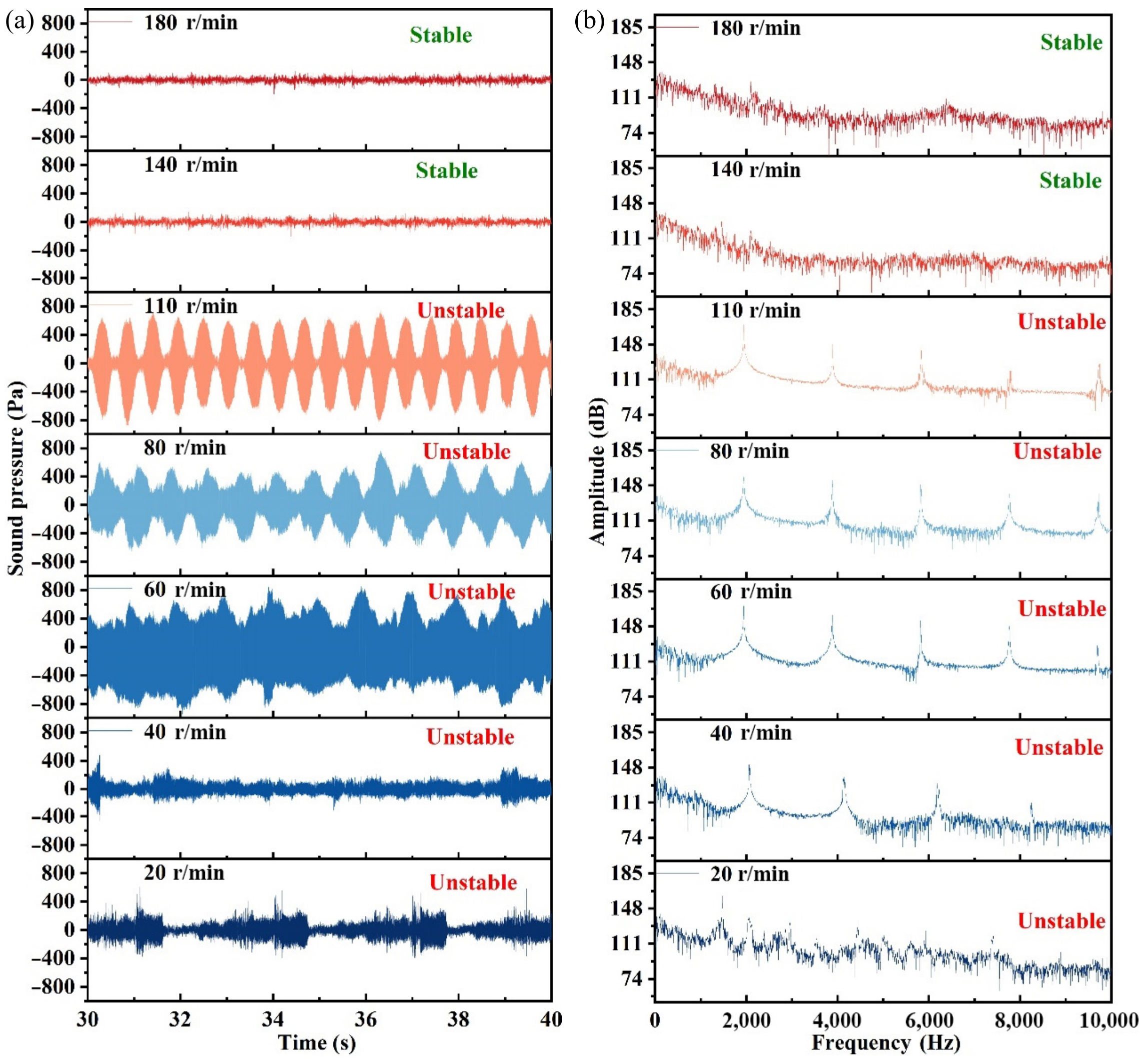

Fig. 19 Experimental results of friction noise under an external load of 0.2 MPa: (a) time domain and (b) frequency domain.

Furthermore, as observed in Fig. 20(a), the predicted horizontal acceleration is divergent at rotational speeds ranging from 20 to 60 r/min, while it appears to be convergent at 80 and 110 r/min. This is because as the rotational speed increases, $\lambda_{\max}$ gradually decreases, and the instability of friction-induced vibration weakens. It can be inferred that the horizontal acceleration at 80 and 110 r/min will gradually diverge over time. Unlike the horizontal acceleration, the horizontal displacement exhibits divergence across all cases when the rotational speed ranges from 20 to 110 r/min, as shown in Fig. 20(b). These numerical results are consistent with the frictional noise measurements presented in Fig. 19.

Table 5 summarizes the maximum attenuation indexes predicted by the numerical model under various rotational speeds and external loads. Notably, the symbols "Y" and "N" in Table 5 indicate the presence and absence of frictional noise observed in the experiments, respectively. The predicted results show good agreement with the experimental observations: frictional noise occurs when the predicted maximum attenuation index is positive. As shown in Fig. 21, the critical rotational speed at which unstable friction-induced vibration does not occur increases with the specific pressure, which is consistent with the result shown in Fig. 16(a). In general, the validity of the theoretical model proposed in this study is demonstrated through an indirect comparison between the results of complex modal analysis and frictional noise experiments.

4 Conclusions

In this study, a 3-DOF friction-induced vibration model was developed for WLBs. The model accounts for the stiffness and damping coefficients of the water film, as well as the contact stiffness of the rough surface. Subsequently, complex eigenvalue analysis was conducted to assess the stability of friction-induced vibration, and the predicted results were validated against experimental observations for a WLB under various combinations of rotational speed and external load. Based on the developed model, the effects of key parameters, including radial clearance, groove width, boundary friction coefficient, and surface roughness, on the stability of the WLB were systematically investigated. The conclusions are as follows:

(1) The boundary μ_c and surface roughness σ significantly affect the stability of friction-induced vibration in WLBs. As μ_c and σ increase, the risk of unstable friction-induced vibration also increases. For the current simulation, when μ_c is less than 0.15 and the rotational speed exceeds 400 r/min, the WLB exhibits frictional stability under external loads ranging from 500 to 8,000 N. When σ exceeds 1.8 μm, the WLB system still poses a risk of unstable friction vibration even at a rotational speed of 1,000 r/min.

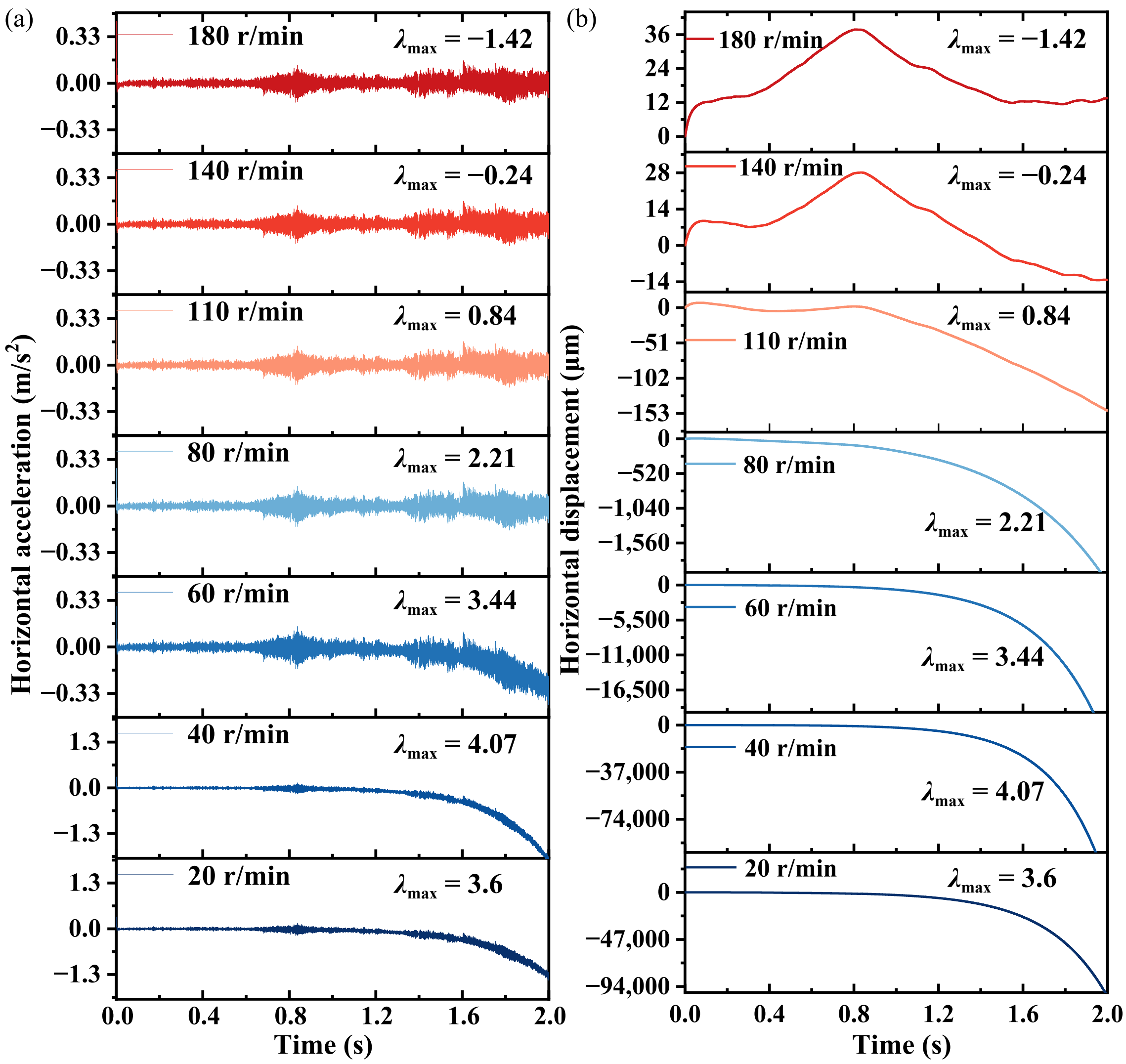

Fig. 20 Simulation results of current model under an external load of 0.2 MPa: (a) horizontal vibration and (b) horizontal displacement.

Table 5 Maximum attenuation index under different external loads and rotational speeds

	20 r/min	40 r/min	60 r/min	80 r/min	110 r/min	140 r/min	180 r/min
0.2 MPa	3.60 (Y)	4.07 (Y)	3.44 (Y)	2.21 (Y)	0.84 (Y)	−0.24 (N)	−1.42 (N)
0.3 MPa	2.45 (Y)	3.12 (Y)	3.19 (Y)	2.72 (Y)	1.45 (Y)	0.42 (Y)	−0.91 (N)

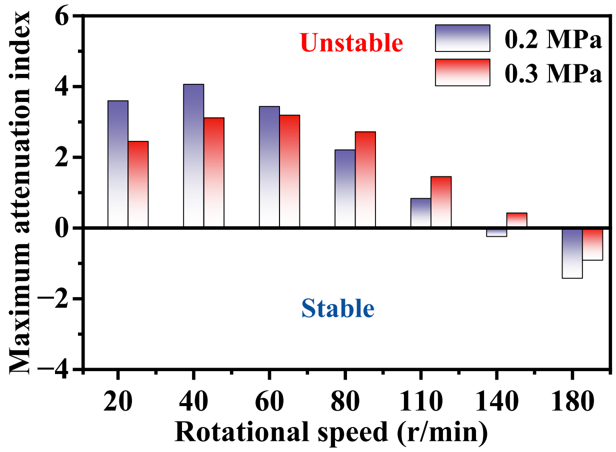

Fig. 21 Variation in maximum attenuation index of tested WLB with rotational speed under three different external loads.

(2) Due to the enhanced asperity contact and the reduction in water film damping, increasing the radial clearance C and groove width W_g elevates the risk of unstable friction-induced vibration. In the present simulation, instability remains evident when the clearance ratio exceeds 0.03% of the journal radius, even at rotational speeds close to 400 r/min. Furthermore, when the groove area is more than twice the load-carrying area, unstable friction-induced vibrations are observed throughout the entire load range of 500–5,000 N.

(3) A critical rotational speed exists at which the vibration transitions from being unstable to stable, and this speed is lower than the lift-off speed. A larger external load corresponds to a higher critical rotational speed. Specifically, the transition speed is 560 r/min, while the lift-off speed is 812 r/min at a specific pressure of 0.5 MPa. Moreover, as the rotational speed approaches this critical value, the unstable friction-induced vibration rapidly diminishes. In the hydrodynamic lubrication regime, the maximum attenuation index remains nearly constant with increasing rotational speed; this value is −30 in the current simulation.

(4) A frictional noise experiment is conducted on the WLB under two external loads and various rotational speeds. The results of the complex eigenvalue analysis show good agreement with the experimental observations, thereby validating the effectiveness of the proposed model.

Journal misalignment is almost unavoidable in marine stern shaft propulsion systems, highlighting the need for further studies on friction-induced vibration in WLBs under misaligned rotors and on three-dimensional structural temperature rise under harsh operating conditions.

Acknowledgements

The author(s) disclosed receipt of the following financial support for the research, authorship, and/or publication of this article: This study was partially supported by the National Natural Science Foundation of China (Nos. 52105052 and 52575067), the Sichuan Provincial Natural Science Youth Foundation (No. 2026NSFSC1239), the China Postdoctoral Science Foundation (No. 2025M781330), and Technology Research Program of Chongqing Municipal Education Commission (No. KJQN202301547).

Availability of data and materials

The data that support the findings of this study are available from the corresponding author upon reasonable request.

Declaration of competing interest

The authors have no competing interests to declare that are relevant to the contents of this article.

References

[1] Zhang Z, Ouyang W, Liang X X, Yan X P, Yuan C Q, Zhou X C, Guo Z W, Dong C L, Liu Z L, Jin Y, et al. Review of the evolution and prevention of friction, wear, and noise for water-lubricated bearings used in ships. *Friction* **12**(1): 1–38 (2024)

[2] Xie Z L, Jiao J, Yang K, Zhang H. A state-of-art review on the water-lubricated bearing. *Tribol Int* **180**: 108276 (2023)

[3] Ning C X, Hu F, Ouyang W, Yan X P, Xu D L. Wear monitoring method of water-lubricated polymer thrust bearing based on ultrasonic reflection coefficient amplitude spectrum. *Friction* **11**(5): 685–703 (2023)

[4] Ouyang W, Zhang Z, Nie Y Z, Liu B, Vanierschot M. Parametric modeling and collaborative optimization of a rim-driven thruster considering propeller-duct interactions. *Ocean Eng* **337**: 121746 (2025)

[5] Ouyang W, Liu Q L, Li J J, Jin Y, Dong X W. Semi-active control for transverse vibration of ship propulsion shafting with magnetorheological squeeze film damper. *Mech Syst Signal Pr* **233**: 112763 (2025)

[6] Avishai D, Morel G. Experimental investigation of lubrication regimes of a water-lubricated bearing in the propulsion train of a marine vessel. *J Tribol–T Asme* **143**(4): 041803 (2021)

[7] Xie Z L, Tian Y X, Liu S M, Ma W S, Gao W J, Du P, Zhao B. Fluid-structure interaction analysis of a novel water-lubricated bearing with particle-dynamic effect: Theory and experiment. *Tribol Int* **204**: 110474 (2025)

[8] Kim W, Lim S H, Hong H, Kang D, Kim W, On S Y, Lee H E, Bae S, Kim S S. Exploring turbulence and elastic deformation: Novel insights into dynamic instability in water-lubricated composite journal bearings for hub-type rim-driven thrusters. *Friction* **13**(8): 9441053 (2025)

[9] Peng E G, Zheng L L, Tian Y Z, Lan F. Experimental study on friction-induced vibration of water-lubricated rubber stern bearing at low speed. *Appl Mech Mater* **44–47**: 409–413 (2010)

[10] Kuang F M, Mu H D, Huang J, Wan G, Yuan C Q, Zhou X C. Theoretical and *in situ* high speed measurement study on friction-induced vibration in water lubricated rubber bearing-shaft system. *Tribol T* **67**(1): 47–61 (2024)

[11] Kuang F M, Zhou X C, Huang J, Wang H, Zheng P F. Machine-vision-based assessment of frictional vibration in water-lubricated rubber stern bearings. *Wear* **426**: 760–769 (2019)

[12] Yang C Z, Kuang F M, Wang T, Chen M X. Friction-induced vibration and noise in water-lubricated stern bearings: A comprehensive review of mechanisms and design. In: Proceedings of the ASME 43rd International Conference on Ocean, Offshore and Arctic Engineering, 2024: V05BT06A053.

[13] Lontin K, Khan M. Interdependence of friction, wear, and noise: A review. *Friction* **9**(6): 1319–1345 (2021)

[14] Tian Y, Khan M, Yuan H, Zheng B H. Wear modeling and friction-induced noise: A review. *Friction* **14**(2): 9441124 (2026)

[15] Chen G X, Zhou Z R, Kapsa P, Vincent L. Experimental investigation into squeal under reciprocating sliding. *Tribol Int* **36**(12): 961–971 (2003)

[16] Thörmann S, Markiewicz M, von Estorff O. On the stick-slip behaviour of water-lubricated rubber sealings. *J Sound Vib* **399**: 151–168 (2017)

[17] Han H S, Lee K H. Experimental verification of the mechanism on stick-slip nonlinear friction induced vibration and its evaluation method in water-lubricated stern tube bearing. *Ocean Eng* **182**: 147–161 (2019)

[18] Qin H L, Yang C, Zhu H F, Li X F, Li Z X, Xu X. Experimental analysis on friction-induced vibration of water-lubricated bearings in a submarine propulsion system. *Ocean Eng* **203**: 107239 (2020)

[19] Butlin T, Woodhouse J. Friction-induced vibration: Model

development and comparison with large-scale experimental tests. *J Sound Vib* **332**(21): 5302–5321 (2013)
[20] Wang D W, Mo J L, Wang Z G, Chen G X, Ouyang H, Zhou Z R. Numerical study of friction-induced vibration and noise on groove-textured surface. *Tribol Int* **64**: 1–7 (2013)
[21] Lin C G, Zou M S, Can S M, Liu S X, Jiang L W. Friction-induced vibration and noise of marine stern tube bearings considering perturbations of the stochastic rough surface. *Tribol Int* **131**: 661–671 (2019)
[22] Lin C G, Zou M S, Zhang H C, Qi L B, Liu S X. Influence of different parameters on nonlinear friction-induced vibration characteristics of water lubricated stern bearings. *Int J Nav Arch Ocean* **13**: 746–757 (2021)
[23] Lin C G, Yang Y N, Chu J L, Can S M, Liu P, Qi L B, Zou M S. Study on nonlinear dynamic characteristics of propulsion shafting under friction contact of stern bearings. *Tribol Int* **183**: 108391 (2023)
[24] Gao K Y, Huang Q W, Xie Z H. Stability analysis of friction self-excited vibration of ship propulsion shaft-bearing system based on modal-coupling mechanism. *J Mech Sci Technol* **39**(5): 2563–2574 (2025)
[25] Ouyang H, Mottershead J E. Dynamic instability of an elastic disk under the action of a rotating friction couple. *J Appl Mech* **71**(6): 753–758 (2004)
[26] Nobari A, Ouyang H J, Bannister P. Uncertainty quantification of squeal instability via surrogate modelling. *Mech Syst Signal Pr* **60–61**: 887–908 (2015)
[27] Chen F, Ouyang H J, Wang X C. A new mechanism for friction-induced vibration and noise. *Friction* **11**(2): 302–315 (2023)
[28] Chen W, Mo J L, Ouyang H J, Zhao J, Xiang Z Y. Suppressing friction-induced stick–slip vibration through a linear PZT-based absorber and energy harvester. *Friction* **12**(7): 1449–1468 (2024)
[29] Wang Q, Wang Z W, Mo J L. A hybrid friction-induced vibration form: Experimental measurement and mechanism discussion. *Tribol Int* **183**: 108397 (2023)
[30] Kang J. Friction-induced noise of gear system with lead screw and nut: Mode-coupling instability. *J Sound Vib* **356**: 155–167 (2015)
[31] Feng H H, Jiang S Y, Ji A M. Investigations of the static and dynamic characteristics of water-lubricated hydrodynamic journal bearing considering turbulent, thermohydrodynamic and misaligned effects. *Tribol Int* **130**: 245–260 (2019)
[32] Guo J, Cohen I, Goltsberg R, Han Y F, Groper M. Assessing Reynolds and Jakobsson–Floberg–Olsson models for infinitely long water-lubricated partial journal bearings: Static and dynamic performance predictions compared to computational fluid dynamics analysis. *Phys Fluids* **36**(12): 123618 (2024)
[33] Ebrat O, Mourelatos Z P, Vlahopoulos N, Vaidyanathan K. Calculation of journal bearing dynamic characteristics including journal misalignment and bearing structural deformation. *Tribol T* **47**(1): 94–102 (2004)
[34] Yamada H, Taura H, Kaneko S. Numerical and experimental analyses of the dynamic characteristics of journal bearings with square dimples. *J Tribol–T Asme* **140**: 011703 (2018)
[35] Ren T M, Feng M. Stability analysis of water-lubricated journal bearings for fuel cell vehicle air compressor. *Tribol Int* **95**: 342–348 (2016)
[36] Ren T M, Feng M. Theoretical and experimental study on the stability of water-lubricated high speed journal bearing with lobe pockets. *Tribol Int* **187**: 108665 (2023)
[37] Feng H H, Gao Z W, Van Ostayen R A J, Zhang X F. A numerical investigation of the effects of groove texture on the dynamics of a water-lubricated bearing–rotor system. *Lubricants* **11**(6): 242 (2023)
[38] Xiang G, Wang Y J, Wang C, Lv Z L. Numerical study on the dynamic characteristics of water-lubricated rubber bearing under asperity contact. *Ind Lubr Tribol* **73**(4): 572–580 (2021)
[39] Kuang F M, Zhou X C, Liu Z L, Huang J, Liu X S, Qian K W, Gryllias K. Computer-vision-based research on friction vibration and coupling of frictional and torsional vibrations in water-lubricated bearing-shaft system. *Tribol Int* **150**: 106336 (2020)
[40] Jin Y, Li R Q, Ouyang W, Liu Z L, Liu Q L, Xiong Q P, Zhou J H. Feature recognition on friction induced vibration of water-lubricated bearing under low speed and heavy load. *J Mar Sci Eng* **11**(3): 465 (2023)
[41] Yang T Y, Xiang G, Cai J L, Wang L W, Lin X, Wang J X, Zhou G W. Five-DOF nonlinear tribo-dynamic analysis for coupled bearings during start-up. *Int J Mech Sci* **269**: 109068 (2024)
[42] Xiang G, Han Y F. Study on the tribo-dynamic performances of water-lubricated microgroove bearings during start-up. *Tribol Int* **151**: 106395 (2020)
[43] Matania O, Heletz S, Klein R, Groper M, Bortman J. Toward diagnostics of water-lubricated bearings of naval vessels by vibration analysis. *Struct Health Monit* **22**(4): 2565–2578 (2023)
[44] Patir N, Cheng H S. An average flow model for determining effects of three-dimensional roughness on partial hydrodynamic lubrication. *J Lubr Technol* **100**(1): 12–17 (1978)
[45] Wu C W, Zheng L Q. An average Reynolds equation for partial film lubrication with a contact factor. *J Tribol–T Asme* **111**(1): 188–191 (1989)
[46] Kogut L, Etsion I. A finite element based elastic-plastic model for the contact of rough surfaces. *Tribol T* **46**(3): 383–390 (2003)
[47] Xiao H F, Sun Y Y, Xu J W. Investigation into the normal contact stiffness of rough surface in line contact mixed elastohydrodynamic lubrication. *Tribol T* **61**(4): 742–753 (2018)
[48] Xiang G, Wang J X, Zhou C D, Shi Y, Wang Y J, Cai J L, Wang C, Jin D, Han Y F. A tribo-dynamic model of coupled journal-thrust water-lubricated bearings under propeller disturbance. *Tribol Int* **160**: 107008 (2021)
[49] Shi X, Polycarpou A A. Measurement and modeling of normal contact stiffness and contact damping at the meso scale. *J Vib Acoust* **127**(1): 52–60 (2005)
[50] Shi F H, Wang Q J. A mixed-TEHD model for journal-bearing conformal contacts: Part I: Model formulation and approximation of heat transfer considering asperity contact. *J Tribol-T Asme* **120**(2): 198–205 (1998)
[51] Litwin W. Experimental research on water lubricated three layer sliding bearing with lubrication grooves in the upper part of the bush and its comparison with a rubber bearing. *Tribol Int* **82**: 153–161 (2015)
[52] Hamrock B J, Schmid S R, Jacobson B O. *Fundamentals of Fluid Film Lubrication*. Boca Raton (USA): CRC Press, 2004.
[53] Den H, Jacob P. *Strength of materials*. Mineola (USA): Courier Corporation, 2012.
[54] Sol H, Rahier H, Gu J. Prediction and measurement of the damping ratios of laminated polymer composite plates. *Materials* **13**(15): 3370 (2020)
[55] Wang H J, Liu Z L, Zou L, Yang J. Influence of both friction and wear on the vibration of marine water-lubricated rubber bearing. *Wear* **376**: 920–930 (2017)
[56] Heberley B D. Advances in hybrid water-lubricated journal bearings for use in ocean vessels. Ph.D. Thesis. Cambridge (UK): Massachusetts Institute of Technology, 2013.
[57] Khonsari M M, Kim H J. On thermally induced seizure in journal bearings. *J Tribol–T Asme* **111**(4): 661–667 (1989)
[58] Tiwari A, Dorogin L, Tahir M, Stöckelhuber K W, Heinrich G, Espallargas N, Persson B N J. Rubber contact mechanics: Adhesion, friction and leakage of seals. *Soft Matter* **13**(48): 9103–9121 (2017)

Guo Xiang received his Ph.D. degree in Mechanical Engineering from Chongqing University, China, in 2020. He is currently an Associate Professor at the School of Mechanical Engineering, Southwest Jiaotong University, China. His research interests include elasto-plastic contact mechanics, adhesive wear, hydrodynamic lubrication, etc. He has authored more than 40 technical papers and applied for 14 invention patents. He has received honors such as the HIWIN Excellent Doctoral Thesis Award and the First Prize in National Defense Technology Invention.

Jiliang Mo received his M.S. and Ph.D. degrees in mechanical design and theory from Southwest Jiaotong University, China, in 2003 and 2008, respectively. His current position is a professor at Southwest Jiaotong University, China. His research interests include tribology/dynamic behavior analysis, vibration and noise control, and fault diagnosis and intelligence.

Huajiang Ouyang received his B.Eng. degree in 1982, M.Eng. degree in 1985, and Ph.D. degree in 1989 from Dalian University of Technology, China. He is a professor in the School of Engineering, University of Liverpool, UK. He is currently a full-time professor at the School of Mechanical Engineering, Southwest Jiaotong University, China, and a Distinguished Professor of the Changjiang Scholars Program. His research interests include friction-induced vibration, moving-load dynamics, vibration-based structural identification and energy harvesting, and vibration control.

Michel Fillon has been retired from CNRS and Pprime Institute, France, since January 2022. He has been a CNRS director of research at the Pprime Institute, University of Poitiers. From 2002 to 2010, he was a manager of the "Lubricated Contact Mechanics" research group. His research interests were (still are) both experimental and theoretical investigations of hydrodynamic journals and thrust bearings. He is a fellow of ASME and STLE. From May 2016 to May 2021, he was a director of the STLE Board of Directors. He was a member of the Annual Meeting Program Committee of STLE (from 2010 to 2018) and chair of the 73rd STLE Annual Meeting in May 2018 (Minneapolis); he has also organized nine EDF/Pprime Workshops on Journal and Thrust Bearings from the first one in 2002 to 2017. He has been coeditor-in-chief of *Tribology International* (from October 2014 to December 2021) and an associate editor of *ASME Journal of Tribology* (from 2003 to 2009). He is currently coeditor-in-chief of *Mechanics & Industry* and associate editor of *Lubricants* as well as editorial board member of several other journals. From 2006 to 2008, he was the chair of Research Committee of ASME Tribology Division and from.

Guangwu Zhou received his master and Ph.D. degrees from Chongqing University, China, in 2010 and 2013, respectively. After completing his Ph.D. degree, he joined the School of Aeronautics and Astronautics at Sichuan University, China, where he has served as an associate professor since 2016. His main research interests include transmission tribology, water-lubricated bearing technology, and the optimal design of precision reducers for industrial robots.

Liwu Wang received his Ph.D. degree from the College of Mechanical and Transportation Engineering, Chongqing University, China, in 2025. Currently, he is a postdoctoral fellow at the College of Marine Science and Engineering, Hainan University, China. His main research interests include tribology problems in tropical marine wind power transmission systems and marine equipment transmission.

Changqi Zhou was graduated from Chongqing Technology and Business University, China, with a degree in mechanical and electronic engineering in 2023 and is currently a second-year graduate student at Chongqing University of Science and Technology, China, focusing his research on high-performance electromechanical transmission and intelligent equipment.